



HAL
open science

Modeling the morphological diversity of impact craters on icy satellites

Laurel E. Senft, Sarah T. Stewart

► **To cite this version:**

Laurel E. Senft, Sarah T. Stewart. Modeling the morphological diversity of impact craters on icy satellites. *Icarus*, 2011, 10.1016/j.icarus.2011.04.015 . hal-00768795

HAL Id: hal-00768795

<https://hal.science/hal-00768795>

Submitted on 24 Dec 2012

HAL is a multi-disciplinary open access archive for the deposit and dissemination of scientific research documents, whether they are published or not. The documents may come from teaching and research institutions in France or abroad, or from public or private research centers.

L'archive ouverte pluridisciplinaire **HAL**, est destinée au dépôt et à la diffusion de documents scientifiques de niveau recherche, publiés ou non, émanant des établissements d'enseignement et de recherche français ou étrangers, des laboratoires publics ou privés.

Accepted Manuscript

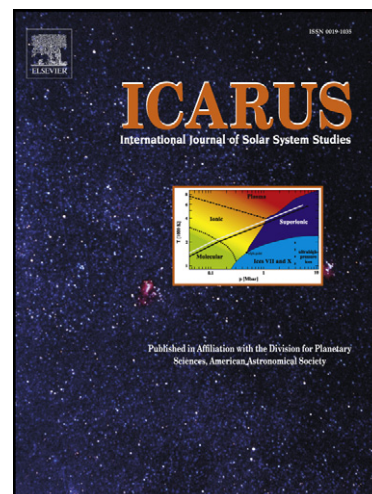
Modeling the morphological diversity of impact craters on icy satellites

Laurel E. Senft, Sarah T. Stewart

PII: S0019-1035(11)00150-3
DOI: [10.1016/j.icarus.2011.04.015](https://doi.org/10.1016/j.icarus.2011.04.015)
Reference: YICAR 9792

To appear in: *Icarus*

Received Date: 4 June 2009
Revised Date: 16 April 2011
Accepted Date: 16 April 2011



Please cite this article as: Senft, L.E., Stewart, S.T., Modeling the morphological diversity of impact craters on icy satellites, *Icarus* (2011), doi: [10.1016/j.icarus.2011.04.015](https://doi.org/10.1016/j.icarus.2011.04.015)

This is a PDF file of an unedited manuscript that has been accepted for publication. As a service to our customers we are providing this early version of the manuscript. The manuscript will undergo copyediting, typesetting, and review of the resulting proof before it is published in its final form. Please note that during the production process errors may be discovered which could affect the content, and all legal disclaimers that apply to the journal pertain.

1 **Modeling the morphological diversity of impact craters on icy satellites**

2 Laurel E. Senft and Sarah T. Stewart

3

4 Department of Earth and Planetary Sciences

5 Harvard University

6 20 Oxford Street

7 Cambridge, MA 02138

8

9 Senft: laurelsenft@gmail.com, 857-998-1685

10 Stewart: sstewart@eps.harvard.edu, 617-496-6462

11

12 Submitted to Icarus June, 2009

13 Revised March, 2011

14 Accepted April, 2011

ACCEPTED MANUSCRIPT

15

16 Manuscript: 40 pages, 13 Figures, and 1 Table

17 Online Supplemental Materials: 2 pages, 1 Table, 2 Figures, 13 Quicktime animations

18

19 Proposed running head: Cratering in ice

20 Direct editorial correspondence and proof to: Sarah Stewart

ACCEPTED MANUSCRIPT

21

22 **Abstract**

23 Impact craters on icy satellites display a wide range of morphologies, some of which have no
24 counterpart on rocky bodies. Numerical simulation studies have struggled to reproduce the diversity of
25 features, such as central pits and transitions in crater depth with increasing diameter, observed on the
26 icy Galilean satellites. The transitions in crater depth (at diameters of about 26 and 150 km on
27 Ganymede and Callisto) have been interpreted as reflecting subsurface structure. Using the CTH shock
28 physics code, we model the formation of craters with diameters between 400 m and about 200 km on
29 Ganymede using different subsurface temperature profiles. Our calculations include recent
30 improvements in the model equation of state for H₂O and quasi-static strength parameters for ice. We
31 find that the shock-induced formation of dense high-pressure polymorphs (ices VI and VII) creates a gap
32 in the crater excavation flow, which we call discontinuous excavation. For craters larger than about 20
33 km, discontinuous excavation concentrates a hot plug of material (>270 K and mostly on the melting
34 curve) in the center of the crater floor. The size and occurrence of the hot plug are in good agreement
35 with the observed characteristics of central pit craters, and we propose that a genetic link exists
36 between them. We also derive depth vs. diameter curves for different internal temperature profiles. In
37 a 120 K isothermal crust, calculated craters larger than about 30 km diameter are deeper than observed
38 and do not reproduce the transition at about 26 km diameter. Calculated crater depths are shallower
39 and in good agreement with observations between about 30 and 150 km diameter using a warm
40 thermal gradient representing a convective interior. Hence, the depth-to-diameter transition at about
41 26 km reflects thermal weakening of ice. Finally, simulation results generally support the hypothesis
42 that the anomalous interior morphologies for craters larger than 100 km are related to the presence of a
43 subsurface ocean.

44

45 Keywords: cratering, ices, Ganymede, Callisto, interiors

46 **1. Introduction**

47 Impact craters are widespread throughout the solar system and are thus useful probes into
48 planetary subsurfaces. The crater morphology resulting from the impact of an asteroid or comet onto a
49 planetary body is primarily a function of the impactor kinetic energy (velocity and mass), the target
50 composition, and the gravity of the target. Because the icy Galilean satellites (Europa, Ganymede, and
51 Callisto) have a similar gravitational acceleration as Earth's moon, it could be expected that craters of
52 the same size on these bodies would show similar morphologies. Yet craters larger than a few km on
53 the icy satellites are generally shallower than their lunar counterparts, lack peak rings, and display
54 unique morphologies (e.g., central pits, central domes, anomalous forms, and palimpsests) that have no
55 lunar counterpart (Bray et al., 2008; Croft, 1981; Croft, 1983; Moore and Malin, 1988; Moore et al.,
56 2001; Moore et al., 2004; Passey and Shoemaker, 1982; Schenk, 1991; Schenk, 1993; Schenk, 2002;
57 Schenk et al., 2004; Schenk and Turtle, 2009; Smith et al., 1979).

58 The major differences between craters on icy satellites and the moon are illustrated by crater
59 depth and diameter measurements and morphological classifications from Schenk (2002), shown in
60 Figure 1. Simple craters on the icy satellites (black dots in Figure 1) show the traditional bowl shape
61 with depth to diameter ratios similar to those for the moon (thick black line). However the transition
62 from simple to complex craters occurs at smaller crater diameters on the icy satellites (2-3 km,
63 Transition I) than for the moon (15 km, (Pike, 1976)). The simple to complex transition scales with
64 gravity and the strength of the surface materials; hence, the difference in Transition I is attributed to the
65 surface composition: rock for the moon and primarily H₂O ice for the icy Galilean satellites. For
66 Ganymede and Callisto, after Transition I, the crater depths increase with diameter (open circles in
67 Figure 1) until a second kink is reached at diameters of about 26 km (Transition II). At Transition II,

68 crater depths become constant or slowly decrease with diameter and the dominant morphology
69 transitions from central peaks to central pits and central domes (crosses in Figure 1). There is no
70 corresponding transition in the lunar depth versus diameter data and no corresponding lunar crater
71 morphologies. For craters larger than about 150 km (Transition III) on Ganymede and Callisto (error bars
72 in Figure 1), crater morphologies become anomalous and extremely shallow. On the Moon, the
73 transition to basins begins around 100-200 km, where central peak morphologies transition to peak-ring
74 morphologies (Williams and Zuber, 1998). However, note that the degree of structural equivalence
75 between basins on the Moon and icy satellites is not well understood. The morphological characteristics
76 for craters on Ganymede and Callisto are essentially the same. However, European craters differ from
77 craters on Ganymede and Callisto, with Transitions II and III occurring at smaller crater diameters (about
78 8 and 30 km, respectively). Furthermore, there are no central pit craters on Europa as almost no craters
79 are preserved in this size range (Schenk and Turtle, 2009).

80 Schenk (2002) proposed that Transition II is a result of a brittle to ductile transition within the
81 solid ice shell and that Transition III is related to the depth to the ocean. He hypothesized that the
82 differences between the crater morphologies on Europa and Ganymede/Callisto are due to a thinner
83 and warmer ice shell and/or a shallower ocean on Europa. Based on preliminary simulations that
84 indicated that a subsurface ocean is breached when its depth is comparable to the transient crater
85 diameter (Turtle and Ivanov, 2002), Schenk estimated the minimum thickness of the solid ice shells to be
86 19-25 km for Europa and about 80 km for Ganymede and Callisto.

87 It is clear that understanding the cratering process on an icy surface will lead to a better
88 interpretation of what causes the unique crater morphologies on the icy Galilean satellites, and better
89 constraints on the internal structures of these bodies. The internal structures of the icy Galilean
90 satellites are of interest because of the presence of subsurface oceans (Showman and Malhotra, 1999;
91 Spohn and Schubert, 2003). In particular, the solid ice shell on Europa may be thin enough to support

92 life in the ocean (Billings and Kattenhorn, 2005; Chyba, 2000). However, the thickness of Europa's ice
93 shell remains the focus of much debate (Billings and Kattenhorn, 2005).

94 Numerical modeling of impact cratering on the icy satellites have been used to infer the
95 minimum depth to Europa's ocean (Turtle and Pierazzo, 2001), to calculate melt production on Titan
96 (Artemieva and Lunine, 2003; Artemieva and Lunine, 2005), and to investigate the crater collapse
97 process in ice (Bray et al., 2008). Turtle and Pierazzo (2001) modeled the early stage of impact and
98 calculated the depths of melting below craters of different sizes and in targets with varying depths to an
99 ocean. Based on the assumption that central peaks cannot form in craters where the melt zones
100 penetrate to the subsurface ocean, they constrained the crust to be at least 3 to 4 km thick. Bray et al.
101 (2008) simulated the formation of approximately 20-km diameter craters on Ganymede to fit the
102 parameters for different strength-weakening models that control the final stage of crater formation.
103 They found that the strength-weakening parameters for Ganymede are similar to those fitted to the
104 moon. Additionally, Artemieva and Lunine (2003; 2005) used 3D numerical simulations of the early
105 stages of impacts onto ice to estimate the amount of liquid water that may have been generated on the
106 Saturnian moon Titan. They found that very early on in Titan's history, a global liquid layer may have
107 been present, but at later times, impact-generated liquid was local and transient.

108 Accurate modeling of crater formation in ice requires a robust equation of state and
109 temperature-dependent strength model. The major limitation of previous studies of cratering in ice has
110 been the equation of state (EOS) model. In general, EOS models for H₂O (such as ANEOS (Thompson and
111 Lauson, 1972; Turtle and Pierazzo, 2001), Mie-Grüneisen, and Tillotson (Appendix II in Melosh, 1989)
112 have been highly simplified, neglecting the high-pressure solid phases and inaccurately representing
113 phase boundaries.

114 In this work, we model the formation of impact craters with diameters between 400 m and
115 about 200 km on Ganymede using different subsurface temperature profiles. The simulations utilize a

116 new EOS model for H₂O, the 5-Phase EOS, which includes high-pressure solid phases and accurate
117 melting and vaporization curves. We model the entire cratering process, from impact to final
118 morphology, using an updated rheological model for ice. The goals of this study are to (1) improve our
119 understanding of the mechanics of crater formation in ice (including the sensitivity to the EOS and
120 strength model) and (2) to identify the process(es) that lead to the diversity of crater morphologies on
121 icy satellites.

122

123 2. Method

124 We conducted two-dimensional, axisymmetric simulations of crater formation on Ganymede.
125 The projectile and targets were composed of pure H₂O. While Ganymede (surface gravity of 1.43 m/s²) is
126 believed to be differentiated (with a nearly pure H₂O surface), Callisto's (1.32 m/s²) internal structure is
127 more ambiguous (e.g., Schubert et al., 2004). The results of this work also apply to Callisto if its crust is
128 predominantly composed of H₂O ice. Projectile diameters ranged from 10 m to 20 km. The nominal
129 impact velocity was 15 km/s, similar to estimates of the mean impact velocities on the icy Galilean
130 satellites (21 km/s on Ganymede and 16 km/s on Callisto for the impact of Jupiter family comets, which
131 comprise >90% of impactors on these satellites (Zahnle et al., 1998)). Final crater (rim-to-rim) diameters
132 ranged from 400 m to about 200 km.

133 We varied the internal temperature profile of Ganymede. The surface temperature was
134 assumed to be 120 K (approximately the equilibrium mid-latitude surface temperature). Two thermal
135 profiles were considered: an end-member "cold" isothermal crust and a "warm" thermal gradient to
136 represent a convective interior. The warm case is assumed to have a gradient of 20 K/km through the
137 lithosphere (6.5 km thick) and a convecting ice interior at 250 K. These temperature profiles are
138 consistent with estimates of the early thermal gradient and lithospheric thickness on Ganymede
139 (Golombek and Banerdt, 1986; Luttrell and Sandwell, 2006). Two sets of simulations were also

140 conducted with the added complexity of a 275 K ocean at depths of 25 and 50 km, below the convective
141 lid (at 250 K). The ocean extends to the bottom of the computational mesh. We model the boundary
142 between the convective ice and the ocean as an abrupt transition; in actuality, the boundary layer
143 should have a small width (Schubert et al., 2004). The projectile temperature was 120 K in all cases.

144 Cratering simulations were conducted using the widely-used CTH shock physics code (version 8)
145 (McGlaun et al., 1990), which we have extended to include strength models appropriate for planetary
146 impact problems (Senft and Stewart, 2007). The resolution of the computational mesh is fixed in the
147 region of crater formation, and the resolution is allowed to increase in the margins of the calculation
148 domain using the adaptive mesh refinement feature (Crawford, 1999). The maximum resolution of
149 each simulation was at least 40 cells across the diameter of the projectile. Massless, Lagrangian tracer
150 particles are embedded in horizontal rows to track the stratigraphic deformation and thermodynamic
151 histories of the target material.

152 We utilize the quasi-static strength model of Collins et al. (2004) (Senft and Stewart, 2007; Senft
153 and Stewart, 2008). In this model, a pressure-dependent shear strength is degraded from an intact
154 curve to a damaged (fractured curve) with the accumulation of damage (which is a function of
155 integrated plastic shear strain). The shear strength is thermally degraded with a pressure-dependent
156 melting curve that matches the melting curve for H₂O ice. Tensile strength is also degraded with
157 damage, and void is added under tensile failure to simulate fracturing. The strength parameters for ice
158 are derived in Senft and Stewart (2008) by fitting to experimental data on the quasi-static shear
159 strength, friction, and dynamic tensile strength. The parameters are slightly modified from Senft and
160 Stewart (2008) to better match the colder temperatures on Ganymede compared to Mars (see Table 1).

161 To achieve the appropriate amount of collapse, a transient weakening mechanism is needed for
162 complex craters. The weakening process is still debated (Senft and Stewart, 2009); however, the specific
163 model should not affect the general results presented in this paper (see Section 4.4). We use the block

164 model approximation (Melosh and Ivanov, 1999) of acoustic fluidization (Melosh, 1979), whereby
165 acoustic waves generated by the impact periodically increase and decrease the overburden pressure
166 (temporarily allowing the material to fail). Averaged over time, the bulk rheology of the weakened
167 material is approximated by a Bingham plastic (a material that behaves as a rigid solid below the yield
168 stress, but as a viscous fluid above the yield stress). The effective viscosity and a decay time
169 (representing the characteristic decay time of the acoustic waves) are the two main parameters of the
170 model. Because the acoustic fluidization parameters are unconstrained by laboratory experiments, they
171 are generally chosen by fitting to observed crater depth versus diameter curves (e.g., Collins, 2002;
172 Wünnemann and Ivanov, 2003). However, using this method to choose parameters for Ganymede
173 (tweaking the parameters until a perfect match is reached) would obscure the effect of other variables,
174 such as the thermal profile and equation of state. There is no physical reason for greatly different
175 acoustic fluidization parameters in ice and rock, and a recent study (Bray et al., 2008) argues that the
176 crater collapse process is similar on Ganymede and the moon based on the gross similarity in complex
177 crater morphologies for diameters less than 12 km. The same study successfully reproduced the
178 observed morphology of approximately 20-km diameter Ganymede craters using acoustic fluidization
179 parameters similar to the moon (no other sizes were modeled). Thus, in this work, we used acoustic
180 fluidization parameters as determined for the moon (Wünnemann and Ivanov, 2003).

181 The projectile and target were modeled using the tabular 5-Phase equation of state (EOS) for
182 H₂O (Senft and Stewart, 2008). This EOS has been validated with experimental data (Senft and Stewart,
183 2008; Stewart et al., 2008). The 5-Phase EOS includes three solid phases (ices Ih, VI, and VII), liquid, and
184 vapor. In reality, H₂O forms at least 11 stable phases (Petrenko and Whitworth, 1999); however, some
185 phases are not created during shock compression (Stewart and Ahrens, 2005). Hence, the model EOS
186 artificially extends the ice VI region to include the ice II, V, and III regions and the ice VII region to
187 include the ice VIII region. The EOS of the phases and unmodified phase boundaries are experimentally

188 determined; for more details see the Appendix and Senft and Stewart (2008). Note that the EOS as
189 presented in Senft and Stewart (2008) contains liquid and solid (ice Ih) tension regions which overlap in
190 temperature versus density space with regions of liquid-vapor and ice Ih-vapor equilibrium,
191 respectively. Since we are interested in the late stage evolution of material on the phase boundaries,
192 we have removed the tension regions from the table (the boundaries are now pure equilibrium). At
193 present, we are unable to model in a single simulation both the release into tension behind the shock
194 wave at early times and the (quasi-)equilibrium compression/decompression of material during crater
195 collapse. We conducted tests to compare cratering simulations with and without tension. The crater
196 formation process and resulting crater sizes were indistinguishable, although the thermodynamic paths
197 of the material are different at early times. The equilibrium table (no tension) is more appropriate for
198 the processes discussed in this work. The EOS does not include phase change kinetics (see discussion in
199 section 4.4).

200 For comparison, we present a simulation using a Mie-Grüneisen equation of state for ice Ih. This
201 EOS does not include any phase changes and utilizes a constant specific heat capacity to calculate
202 temperature. Hence, the temperatures are unreliable. The Mie-Grüneisen EOS (appendix in Melosh,
203 1989) parameters are: 930 kg/m^3 for the initial density, 3 km/s for the bulk sound speed, 1 for the linear
204 slope between shock velocity and shock particle velocity, 1 for the Grüneisen parameter, and $1.98\text{e}17$
205 J/kg/K for the specific heat capacity. This EOS allows material to go into tension and the same strength
206 model is used as in the 5-Phase EOS simulations.

207 In all simulations, very low density material ($<0.0001 \text{ g/cm}^3$) is discarded to allow for reasonable
208 time steps during the calculation.

209

210 3. Results

211 3.1 Discontinuous Excavation: Phase Changes and Hot Plug Formation

212 This work is the first to use a H₂O equation of state with high-pressure solid phases in
213 simulations of crater formation on icy satellites. We find that the shock-induced formation of dense
214 high-pressure polymorphs creates a discontinuity in the excavation flow. Over a certain size range, the
215 highly-shocked material that is interior to the discontinuity is concentrated in a hot, partially liquid plug
216 in the crater floor during crater collapse. This previously unrecognized phenomenon, which we call
217 *discontinuous excavation*, arises from the exceptional polymorphism of H₂O.

218 The differences between discontinuous excavation and classical crater excavation are illustrated
219 in the simulations shown in Figure 2 and the schematic in Figure 3. Figure 2 presents a time series from
220 a simulation of a 2-km diameter projectile impacting at 15 km/s onto a 120 K isothermal Ganymede
221 crust. The final crater is about 39 km in diameter. The left column presents the results using the 5-
222 Phase EOS; the right column presents the results using a Mie-Grüneisen EOS. Initially horizontal rows of
223 tracer particles (black dots and lines in 2A-D and 2F-I) display the stratigraphic deformation. Animations
224 are available in the online supplemental material.

225 The simulation using the Mie-Grüneisen EOS illustrates classical crater excavation (Figure 2F-J)
226 (c.f. Melosh, 1989). After the initial contact and compression stage, the shock wave travels through the
227 target as a hemispherical shell of high pressure and density (called the detached shock, Figure 2F). The
228 material behind the shock wave is released to ambient pressure, setting up the classical excavation flow
229 field that generates a hemispherical transient crater and inverted cone ejecta curtain (Figure 2G and
230 2H). The transient crater collapses under the force of gravity, and the transiently weakened material
231 (from acoustic fluidization) flows inward and upwards, producing a shallow final crater with uplifted
232 stratigraphy beneath the crater floor (Figure 2I). The deep narrow line of hot temperature material
233 presented in Figure 2J represents the characteristic width of artifacts that arise along the center line in a
234 two-dimensional axisymmetric calculation. Recall that the temperatures calculated with the Mie-
235 Grüneisen EOS are unrealistic.

236 In contrast, the time series for the simulation using the 5-Phase EOS displays a gap, or
237 discontinuity, in the excavation flow field. The amplitude of the shock wave decays during propagation
238 into the target. As a result, ice Ih is shocked to progressively lower pressure (and temperature) phases
239 with increasing distance from the impact point. The phase in the shocked state is a supercritical fluid at
240 the impact site, followed by liquid, then high-pressure ice phases (ices VII and VI), and finally simply
241 shock-compressed ice Ih with increasing distance (Figures 2A and 3A).

242 Rarefaction waves from the free surfaces decompress the shocked material. During impact
243 cratering in ice, the release wave travels through layers of different phases, with a strong impedance
244 contrast (density times sound speed) at the liquid-ice VII and ice VI-ice Ih boundaries. The impedance
245 mismatch leads to wave reflections that generate the discontinuity in the excavation flow at the ice VI-
246 ice Ih boundary. In addition, because transformation from the high-pressure solid phases back to ice Ih
247 requires a large volume increase (e.g., about 30% from ice VI to ice Ih), full release of the high-pressure
248 polymorphs is delayed until the volume change can be accommodated in the excavation flow. Thus in
249 Figure 2A, the shock front has proceeded to about 12 km away from the surface, but material far behind
250 the shock wave remains at high density and pressure (red shell). As the excavation flow relieves the
251 overburden pressure, the transformation back to ice Ih occurs progressively from the free surface to
252 greater depths. The time history of an example parcel of material compressed to ice VI is shown on a
253 pressure-temperature phase diagram in Figure 4A (corresponding to the triangle symbol in Figure 2A-D).
254 This parcel was shocked to ice VI and then released to the (artificial) ice Ih-VI phase boundary where it
255 remained for several seconds; the material eventually transformed into ice Ih and decompressed to the
256 sublimation curve before being re-compressed during crater collapse.

257 The large differences in the shock loading and unloading paths between adjacent material
258 shocked to different phases disrupts the excavation flow (see Appendix). In addition, the impedance
259 mismatch between the high pressure ice phases and lower-density phases (supercritical fluid and ice Ih)

260 produce wave reflections that aid in the deceleration of the most highly shocked material. The net
261 effect of these processes is that the fully released particle velocities of the material shocked to high
262 pressure phases are slower than the material shocked within the ice Ih field (exterior to the
263 discontinuity). As a result, the most highly shocked material does not follow the main excavation flow,
264 but lags behind, leading to the formation of a gap in the flow field (see Figures 2B and 2C). The material
265 adjacent to the gap intersects the sublimation curve while decompressing to the low ambient pressure,
266 producing the vapor in the gap (gray material in Figure 2B).

267 Rather than lining the transient crater cavity (as in Figure 2H), the highly shocked material is
268 decelerated and remains temporarily suspended within the transient crater (Figure 2C). This material
269 slowly falls to the crater floor and is compressed by the collapsing crater walls, forming a central plug in
270 the crater floor (Figure 2D and 3C). This central plug is composed of material that was shocked to ice VI,
271 ice VII, and supercritical fluid. Note that, in this example, the material within the central plug is near its
272 original depth rather than forming a broad centrally uplifted zone (as in Figure 2I). We refer to the
273 stratigraphic discontinuity as the central plug. Within the central plug is a smaller plug of hot material
274 that lies on the melt curve (Figures 2E and 3C). We define the hot plug of material by the 270 K
275 temperature contour. Because of the varying pressure field during crater collapse, material near the
276 liquid phase boundary tends to fluctuate above and below the boundary. The fluctuations are probably
277 accentuated by the use of a tabular equation of state. Hence, it is difficult to reliably calculate the exact
278 amount of material that reaches the melting point. In the simulations, the volume of material with
279 temperatures above 270 K remained fairly constant and at times nearly identical to the volume of
280 material above 273 K. An example time history for a parcel of hot plug material is presented in Figure
281 4B (corresponding to the square symbol in Figure 2A-D). In this case, the parcel initially releases to the
282 saturation vapor curve and continues to cool and decompress by creating vapor (as observed

283 experimentally in Stewart et al. (2008)). In this case, the material is recompressed by collapsing to the
284 ground after passing through the triple point.

285 Note that the width of the hot plug (~16 km) is much larger than the center line artifact (~2 km)
286 observed in Figure 2J. Thus, while some of the material in the hot plug in the 5-Phase EOS calculation
287 may be produced because of a centerline artifact, the majority is not. The mass of the hot plug depends
288 on the impact energy and the impact velocity (see section 4.2). If the velocity is too low, then the peak
289 pressures generated by the impact will not be high enough to induce (incipient) melting. However, as
290 the impact velocity increases, the pressure decay profile becomes steeper (Pierazzo et al., 1997)
291 (because more energy is portioned into vaporization), leading to smaller hot plugs. Because crater size
292 is related to impact energy, the mass of the hot plug also scales with the crater diameter (Figure 5). The
293 hot plug volume is only slightly sensitive to initially cold and warm thermal profiles.

294 These simulations utilize a simplified phase diagram for H₂O and assume equilibrium behavior
295 upon release of the high-pressure phases. These limitations will be discussed in section 4.4.

296 The general phenomenon of discontinuous excavation has been observed in previous
297 simulations of impact cratering in layered targets (Ormo et al., 2002; Senft and Stewart, 2007; Senft and
298 Stewart, 2008). For example, impacts through an ocean or ice layer generated nested craters and ejecta
299 curtains. In these previous studies, the discontinuous excavation arose from pre-existing impedance
300 contrasts in the target. In this study, the discontinuous excavation flow occurs in an initially
301 homogenous target and arises from shock-induced phase changes during the impact event.

302 **3.2 Depth vs. Diameter**

303 Our simulations of crater formation utilize independently derived input parameters: quasi-static
304 strength parameters determined by laboratory experiments, acoustic fluidization parameters fitted to
305 lunar data, and an equation of state based on laboratory data. Thus, these simulations of impact
306 cratering in ice are predictive rather than fitted to observations. We find that the final geometries of

307 the simulated craters are in good agreement with observations. In Figure 6, we compare the depth of
308 the simulated craters to measurements of craters on Ganymede and the moon. The shaded area
309 represents the scatter in the measurements from Schenk (2002) (Figure 1B; shaded area does not
310 include error bars on the data points). Our simulated crater geometries lie within or adjacent (within
311 the error bars) to the observed scatter in the observations (with differences in thermal profiles
312 discussed below).

313 To calculate the depths and diameters for the simulated craters, we define the topographic
314 profile by identifying cells with 50% of full density. The rim-to-rim diameter is determined by finding the
315 highest rim point, and the rim-to-floor depth is determined by subtracting the deepest floor point from
316 the highest rim point (ignoring obvious small-scale blips in the topography). Because we use the
317 deepest floor point and not an average over some area of the crater floor, our measurements should be
318 slightly biased toward deeper depths compared to values derived from lower spatial resolution
319 observations (and ignoring post-formation modification). The slightly shallower simulated simple
320 craters may be the result of a quasi-static shear strength that is larger than reality (which limits
321 penetration of the projectile) or too much slumping of the crater walls (e.g., quasi-static shear strength
322 that is weaker than reality). The depths of large craters are sensitive to the initial thermal gradient
323 because of the temperature-dependent shear strength.

324 **3.3 Cold vs. Warm Thermal Profiles**

325 The geometry of craters smaller than about 30 km is not sensitive to the cold vs. warm thermal
326 profile (Figure 6). We do not consider the 0.1 km difference significant for the 3-km diameter cases. For
327 larger craters, there are significant differences between craters formed in the cold versus the warm
328 thermal profiles. Examples of crater formation by a 5-km diameter projectile impacting at 15 km/s are
329 shown in Figure 7; the final crater diameters are about 105 and 145 km for the cold and warm thermal
330 gradient cases, respectively. The phenomenon of discontinuous excavation is also clearly seen in these

331 larger impact craters (note that the first time step at 45 seconds is after full release of the high pressure
332 phases). For the crater formed in the cold case, the central plug falls to the crater floor and is not
333 uplifted much during crater collapse. Uplift occurs around the plug, and part of the plug is squeezed
334 upwards as the walls collapse (Figure 7; 200 and 400s).

335 In contrast, the central plug falls more quickly to the crater floor in the warm thermal gradient
336 simulation. A smaller volume of high pressure phases forms during shock compression at higher initial
337 temperatures. The slightly different loading and release paths lead to a smaller velocity difference at
338 the discontinuity in the warm case. The most highly shocked material then partially lines the transient
339 crater cavity. A very large central peak is created that overshoots the original surface level and then
340 collapses, going through a few oscillations before crater formation is complete. Note that the
341 oscillations in the large central peak effectively mix the original stratigraphy over a wide and deep region
342 in the crater floor. In addition, the most highly shocked material is not resting at the surface.

343 The enhanced collapse in the warm thermal gradient, ultimately forming a larger shallower
344 crater compared to the cold case, is a result of the strong temperature dependence on the strength of
345 ice at relatively low confining pressures. We use a hyperbolic tangent form for the strength reduction;
346 as a result of this dependence, the strength at 210 K is about half the strength at 120 K, and the strength
347 at 250 K is about 17% the strength at 120 K.

348 **3.3 Subsurface Oceans**

349 Adding a subsurface ocean greatly increases the complexity of the cratering process. Example
350 simulations with a subsurface ocean at 25 and 50 km depth are shown in Figure 8 (note that the ice lid
351 overlying the ocean has a warm thermal gradient). In these cases, a 10-km diameter projectile
352 impacting at 15 km/s produces very large final craters, but the rim is difficult to define. Note that
353 discontinuous excavation is evident and affects the flow field in the solid portion of the satellite,
354 although this phenomenon is secondary to the crater collapse process in controlling the final crater

355 morphology. Discontinuous excavation is not observed in the ocean portion of the impacted material
356 because liquid H₂O does not shock to solid phases in a single shock event (Stewart and Ahrens, 2005).

357 When the boundary between the icy crust and the ocean is breached (Figure 8A), or when
358 excavation reaches the ice/water boundary (Figure 8F), the floor rebounds upwards dramatically (Figure
359 8B and 8G). The overshooting central peak then collapses with enough energy to form a second cavity
360 (Figure 8C and 8H). Next, solid ice collapses in from the sides to fill this second cavity (Figure 8C and
361 8H). In contrast to terrestrial cratering, the melt produced in icy impacts is negatively buoyant; hence,
362 the most highly shocked material sinks below the solid layer during collapse of the walls of the second
363 cavity. Note that the exact morphology of the sinking material is probably affected by center line
364 artifacts.

365 The center of the crater continues to oscillate long after the time of impact. As a result, the
366 calculation is more susceptible to errors introduced by the boundaries in the simulation. Furthermore,
367 the observed topography of anomalous basins on icy satellites is also affected by the long term cooling
368 and freezing of the disrupted near-surface layers and viscous relaxation (although the latter probably
369 only applies to the oldest craters (Dombard and McKinnon, 2000; Schenk et al., 2004)). For these
370 reasons, it is difficult to derive a robust depth for comparison to observations, and the ocean
371 simulations are not plotted on Figure 6. It is possible that anomalous craters may also be produced
372 before the ocean is penetrated. Further investigation of the effect of oceans on crater morphology is
373 left for future work.

374 In general, the subsurface ocean simulations support the hypothesis that final crater depths
375 should be shallower due to the accentuated crater collapse when the ocean is breached compared to
376 crater formation completely within the solid surface layer.

377

378 **4. Discussion**

379 **4.1 Transitions in Crater Depth vs. Diameter**

380 Schenk (2002) observed three transitions in the depth versus diameter curves for craters on the
381 icy satellites. The first transition (Transition I) is the simple to complex crater transition, when gravity
382 starts to dominate the crater collapse process (as opposed to material strength). The second transition
383 (Transition II) marks a change in the depth versus diameter curves from increasing depth with diameter
384 to constant or slightly decreasing depth with diameter. Our simulations show that depths continue to
385 increase with diameter in a cold isothermal crust; however, for a warm thermal gradient, there is a
386 rollover in the depth versus diameter curve, and depths began to decrease with diameter (Figure 6).
387 This rollover is caused by the strong dependence of ice strength on temperature. Schenk interpreted
388 Transition II to result from a ductile layer at depth. Note that because of the differences between
389 strength models used in cratering studies versus planetary interior models, it is difficult to relate our
390 results to an abrupt transition to a ductile layer at depth. On Europa, Transition II occurs at smaller
391 crater diameters than it does on Ganymede and Callisto, and the decrease in crater depth with
392 increasing diameter following the transition is steeper. These differences are probably a result of a
393 steeper thermal gradient on Europa.

394 Transition III is thought to result from the influence of an ocean at depth (Schenk, 2002). While
395 it is impossible to compare our simulations with a subsurface ocean directly to observations of depths
396 and diameters, our results show that when craters are large enough compared to the depth to the
397 ocean, the ocean dramatically modifies the cratering process. Thus, our results generally support
398 Schenk's interpretation of the craters on the Galilean satellites.

399 **4.2 Hot Plugs and Central Pits on Icy Satellites**

400 Craters with small, rimmed or rimless central depressions (central pit craters) are common on
401 both Ganymede and Callisto (Figure 9). On Ganymede, central pit craters are seen from about 5 to 100
402 km in diameter (Alzate and Barlow, 2011), and are the dominant crater morphology for craters from

403 about 35 to 60 km in diameter (Schenk et al., 2004). Proposed models for central pit formation
404 generally invoke the actions of ice and/or liquid water during the cratering process. Croft (1981; 1983)
405 suggested that central pits form when the central peak has a large fraction of liquid, which drains away
406 and causes the peak to collapse into a pit. Passey and Shoemaker (1982) hypothesized that ice is too
407 weak to support the weight of large central peaks; thus the peak collapses under its own weight and
408 forms a central pit. Wood et al. (1978) attributed central pits to explosive decompression as ice
409 volatilizes during the impact. Finally, central pits have also been explained as the result of impact into
410 compositionally or rheologically distinct layers at depth (Greeley et al., 1982; Schenk, 1993).

411 Previously suggested hypotheses for central pit formation lacked quantitative measures to
412 compare to observations. Here, we investigate the possibility that central pits are related to the
413 presence of the hot (>270 K) plug that forms during impact cratering in ice. First, we consider the spatial
414 scale of the hot plug feature. There are two potential ways to measure the width of the hot plug: either
415 by measuring the width that extends to depth (labeled A in Figure 3C; results shown in Figure 10A) or by
416 measuring the extent at the surface (labeled B in Figure 3C; results shown in Figure 10B). We find that
417 the ratio of hot plug diameter to crater diameter predicted by the simulations is in good agreement with
418 measurements of the ratio of central pit diameter to crater diameter (Figure 10). Measurements using
419 the first method (Figure 10A) are well within the range of pit diameter to crater diameter ratios (0.11-
420 0.38) for Ganymede, and cluster around the median of 0.19 for craters greater than about 20 km (Alzate
421 and Barlow, 2011). Note that Alzate and Barlow (2011) observe no regional or latitudinal trends in
422 central pit diameter. Schenk's (1993) measurements of pit diameter to crater diameter are also
423 concentrated around 0.2 for crater diameters between about 40 and 70 km and extend up to 0.4 and 0.5
424 for larger craters (120-150 km) on Callisto and Ganymede, respectively. Note that the ratios of the
425 width of the hot plug at the surface to the crater diameter (Figure 10B) are higher than the observed
426 ratios for central pits, and we do not favor comparison between this hot thin layer (see Figure 2E) and

427 central pits. The observed depth of central pits is about 1 km (Bray et al., 2009; Schenk, 1993); if their
428 formation involves draining of liquid water, then the thin layer of hot material, itself about 1 km thick,
429 may have insufficient mass as it is a mixture of melt and ice. Also, we note that the modeled pit to crater
430 diameter may vary slightly with the thermal gradient (and hence, with time); however, we leave this
431 topic for future work.

432 Second, we compare the simulation results to the observed size range of craters with central
433 pits. In the simulations, the mass of the hot plug within craters decreases as a power law with
434 decreasing crater diameter (Figure 5). As a result, the ratio of the plug width to crater diameter is
435 significantly smaller for craters less than about 20 km compared to larger craters (Figure 10). If the hot
436 plug is related to central pits, then the smaller width of the plug for craters less than 20 km is consistent
437 with the observations that central pits are not abundant in smaller craters.

438 Third, we address the question of why central pit craters sometimes appear near central peak
439 craters of a similar preservational state (a proxy for age) and size (Alzate and Barlow, 2011). This
440 observation suggests that the target properties are not likely to solely control central pit formation. If
441 hot plugs are genetically related to central pits, the variability in crater morphologies may result from
442 differences in impactor velocities. In addition to the total impact energy, the mass of the hot plug is
443 sensitive to the impact velocity, as shown in Figure 11. For these simulations, the size of the impactor
444 was varied so that the total kinetic energy was constant; thus, all of the simulations produce similar final
445 crater diameters (for the 15 km/s impact, the projectile was 2 km in diameter, giving final crater
446 diameters of 39.0 and 46.5 km for the cold and warm cases, respectively). At low impact velocities (< 5
447 km/s), the mass of the hot plug drops off dramatically to zero. The formation of hot material by an
448 impact is dependent on the amplitude of the shock pressures and the initial temperature (Stewart et al.,
449 2008). The mass of the hot plug also drops off gradually at very high velocities. In this case, more of the
450 highly shocked material is vaporized rather than melted, and the shock pressures decay more steeply

451 with distance from the impact compared to slower velocities. The velocity dependence for the
452 formation of hot plug material is an example of where the assumption of pure energy scaling in crater
453 formation processes breaks down. Thus, if two adjacent craters of similar age and size have different
454 interior morphologies, then the one without a central pit may have been created by either a very low
455 speed or very high speed impact (relative to the average impact velocity on Ganymede). Note that low
456 impact velocities (<5 km/s) may be achieved by planetocentric secondary impacts, but are unlikely to
457 form craters greater than about 20 km in diameter (Alvarellos et al., 2002). However, comets impact
458 Ganymede at velocities from several km/s to about 30 km/s (Jupiter family comets) and 40 km/s
459 (isotropic comets) (Zahnle et al., 1998). A difference in impact velocity from 10 km/s to 40 km/s can
460 halve the mass of the hot plug (Figure 11).

461 Fourth, there are a series of interesting observations concerning the rimwall structure of central
462 pit craters. The terrace zone of these craters is much less extensive than expected from comparison to
463 similarly-sized lunar craters: the number of terraces is less (one terrace versus several for lunar craters),
464 the rimwall widths are narrower, and the rim heights increase more steeply with diameter (Schenk,
465 1993). Thus the evidence suggests that a mechanism is at work to limit the amount of rimwall failure
466 (Schenk, 1993). During crater formation on a rocky body, the collapsing walls of the crater collide with
467 each other (or the central peak) when they reach the crater center, and this collision limits the amount
468 of rim failure. However, during crater formation in ice, the collapsing walls of the crater collide not with
469 each other, but with the slow-moving central plug. Thus, we speculate that the central plug may act to
470 impede collapse and limit the amount of rimwall failure. This interesting possibility should be
471 investigated in future work.

472 Finally, central pits are a common feature on Ganymede and Callisto rather than on rocky,
473 relatively ice-free bodies like the moon. The formation of the hot plug is directly related to the
474 peculiarities of H₂O and would not be expected on rocky planets. We address the issue of why central

475 pits are found only on certain icy satellites in the next section. The dependence of the hot plug diameter
476 on the crater collapse parameters is discussed in section 4.4.

477 Our results strongly suggest that central pit formation is related to the formation of the hot
478 plug. Because central dome craters are transitional to central pit craters (i.e., both lie on the same
479 depth versus diameter line, with interior morphologies transitioning from pits to domes with increasing
480 crater diameter, and central domes are surrounded by a ridge that is believed to be equivalent to
481 central pit rims), it is likely that the evolution of the hot plug transitions from central pits to central
482 domes at larger diameters (Schenk, 1993). Perhaps this transition is related to the greater fractions of
483 liquid in the hot plug for larger craters. However, the development of the hot plug into a central pit or
484 dome is beyond the scope of this work. As mentioned in previous hypotheses (Croft, 1981), the fact that
485 melt will drain into fractures in the crater floor (a process not modeled in the simulations) may
486 contribute to formation of the pit. Note that Schenk (1993) argued against a liquid water origin for
487 central domes based on the observations that melt lines the crater floor on rocky bodies and that the
488 dome volumes are too large to be refrozen melt. Here we have shown that the unique excavation
489 processes in ice cause the most highly shocked material to be concentrated in a plug at the crater
490 center, instead of lining the crater floor.

491 **4.3 Central Pits on Other Solar System Bodies**

492 To date, amongst the icy satellites, only Ganymede and Callisto have definitive observations of
493 central pit crater morphologies. Craters on Europa lack central pits, with the morphologies transitioning
494 directly from central peaks to anomalous forms (Figure 1). The onset of anomalous forms at smaller
495 diameters has been suggested to be related to the thinner ice shell on Europa compared to Ganymede
496 and Callisto (Schenk, 2002). By the time craters are large enough to form central pits on Europa, crater
497 formation is instead influenced by the presence of a subsurface ocean (Schenk and Turtle, 2009).

498 While the gravity on the largest Saturnian moon Titan (1.35 m/s^2) is similar to the gravity on
499 Ganymede and Callisto, the surface of Titan is actively eroded and preserves very few impact craters
500 (Wood et al., 2010), making it difficult to discern if central pits had formed. The smaller Jovian and
501 Saturnian icy satellites lack craters with definitive central pits, although there are a few possible
502 candidate craters (Schenk, 1993). These candidates show that the onset of central pit morphologies
503 occurs with larger craters on smaller bodies, however the onset does not scale perfectly inversely with
504 gravity (Chapman and McKinnon, 1986; Schenk, 1993). The largest craters on several satellites could
505 have central pit morphologies using simple gravity scaling from Ganymede and Callisto, but instead the
506 craters show central peaks (Chapman and McKinnon, 1986). For example Triton's (0.78 m/s^2 ; Triton is a
507 moon of Neptune and the largest moon beyond Saturn) largest crater is 25 km in diameter. This
508 diameter is larger than a gravity-scaled central pit transition of about 16 km, and yet the crater does not
509 exhibit a central pit.

510 If the formation of central pits is related to the volume of shock-generated melt, as in the model
511 suggested here, then the onset of central pit morphologies should occur with larger craters on smaller
512 icy satellites (because it takes less energy to create a crater of the same size on a smaller body than on a
513 larger body), as observed. However, the formation of pits will not scale perfectly with gravity. As
514 illustrated in Figure 11, the mass of the hot plug is a function of not only the impact energy, but the
515 velocity as well (which determines the peak shock pressure). The dependence on velocity will prevent
516 perfect gravity scaling.

517 While there are as of yet no observations of craters on Pluto, we predict that no central pit
518 craters should exist as a result of the low gravity (0.64 m/s^2) and low impact velocities (average of 1.9
519 km/s (Zahnle et al., 2003)). An observation of large craters on Pluto without central pits (greater than
520 about 60 km diameter by pure gravity scaling from Transition II) would be strong support for a
521 velocity/pressure-dependence for the genesis of central pits. Finally, central pits are also observed in

522 craters on Mars (Barlow, 2006; Barlow, 2007; Barlow, 2009; DeVries and Barlow, 2009; Wood et al.,
523 1978). Unlike the central pits on Ganymede, the Martian pits are observed not only in the bottom of
524 craters, but on the top of central peaks as well. Hence, the formation of Martian pits may or may not be
525 analogous to pits on icy satellites. Hypotheses for Martian pit formation generally involve the presence
526 of subsurface ice rich layers (Barlow, 2006; Barlow, 2007; Barlow, 2009; DeVries and Barlow, 2009;
527 Wood et al., 1978).

528 **4.4 Limitations and Assumptions**

529 In this work, we have focused on aspects of impact crater formation that are unique to high
530 energy impacts onto icy surfaces. The results presented here are principally dependent upon the
531 accuracy of the equation of state model for H₂O and the crater collapse process.

532 *Equation of State*

533 As discussed in section 2, the equation of state model includes five phases. In particular, the ice
534 Ih boundary with ice VI is artificial. The original justification for this simplification in the phase diagram
535 is based on shock wave experiments (Stewart and Ahrens, 2005). The dynamic strength of ice Ih is larger
536 than the phase space between ice Ih and VI. Hence, the first phase transformation on the ice shock
537 Hugoniot is to ice VI, skipping the intermediate phases (ices III, V, and II). The second and third
538 transitions are to ice VII and supercritical fluid, respectively. The uncertainty in the model equation of
539 state primarily arises during the decompression of ice VI and ice VII.

540 Ices VI and VII may decompress metastably to ambient pressures at sufficiently low
541 temperatures (e.g., cooled to 77 K by liquid nitrogen). However, upon heating, ice VI and ice VII will
542 transform to ice Ic (and then later to ice Ih) at about 150 and 120 K, respectively (Bertie et al., 1964).
543 Thus, because shock compression is accompanied by irreversible heating and the initial temperatures in
544 this work were at or above 120 K, we expect the high pressure solid phases to transform back to ice Ih
545 upon decompression. The uncertainty lies in where along the decompression path the transformation

546 takes place. In the equilibrium model, the transformation back to ice Ih occurs at the model phase
547 boundary. In reality, the transformation probably occurs at pressures below the phase boundary
548 because of phase change kinetics. At present, we are unable to model the kinetics of delayed
549 transformations between phases. In the case of ice, it would appear that the equilibrium phase
550 boundaries for ice VI and VII are applicable during shock compression (Stewart and Ahrens, 2005), but
551 that kinetically modified boundaries are more appropriate upon release. Unfortunately, no shock
552 decompression data exist that could define the parameters for a kinetic model.

553 We investigated the sensitivity of hot plug formation to the pressure of the artificial phase
554 boundary between ice Ih and VI. In the nominal phase diagram, the ice Ih-VI boundary is at the actual
555 ice Ih-II and ice Ih-III boundaries, near 200 MPa. In other words, the phase space of ice VI has been
556 extended. For comparison, we constructed a model equation of state with the ice Ih-VI boundary at the
557 actual ice VI phase boundary, near 632 MPa. In this case, the phase space of ice Ih has been extended.
558 Changing the boundary slightly modifies the excavation flow field but does not change the phenomenon
559 of discontinuous excavation. Raising the boundary decreases the amount of central plug material but
560 does not significantly change final crater shape or the amount of hot material within the plug: for a 120
561 K isothermal target with a 2 km diameter impactor, the hot plug mass was 2.5×10^{14} kg with the 200 MPa
562 boundary and 2.8×10^{14} kg with the 632 MPa boundary. Similarly, lowering the phase boundary to 50
563 MPa (to simulate delayed decompression) also does not change the phenomena of discontinuous
564 excavation. Note that most of the material within the hot plug was shocked to pressures greater than
565 ~ 2 GPa (the criteria for incipient melting (Stewart et al., 2008)); hence, the exact location of the ice Ih-
566 ice VI boundary (at lower pressures) is not significant.

567 The phenomenon of discontinuous excavation arises because of the creation of the high-
568 pressure ice phases during shock compression, which has been shown experimentally. The exact
569 volume of high-pressure material depends on the details of the model phase boundary but does not

570 vary significantly for the approximations described here. We conclude that the phenomenon of
571 discontinuous excavation is not an artifact of the model equation of state. It is a robust feature based
572 on the characteristics of H₂O (see Appendix).

573 Finally, coexistence of two phases, such as solid and vapor, is described by an average state
574 (e.g., average density and internal energies) in the tabular EOS. The two phases are treated as a single
575 material. In other words, there is no separation of the phases that could lead to two-phase flow, and the
576 vapor is not allowed to diverge from the solid. The late stage evolution of the hot plug would be more
577 realistically described by a model that allowed for two-phase flow.

578 *Crater Collapse*

579 The depths versus diameters of the simulated craters do not *exactly* match the observations
580 (Figure 6): the simulated simple craters are slightly shallow and the complex craters are slightly deeper
581 than observed. The final crater shape is dependent on both the quasi-static strength model and the
582 crater collapse model. Although the quasi-static strength model is fit to laboratory data, it may not
583 precisely represent an icy planetary crust. Our simulations also assumed a perfectly intact surface (e.g.,
584 no initial fractures).

585 As discussed in section 2, the choice of acoustic fluidization parameters in the crater collapse
586 model is uncertain. The acoustic fluidization model is tunable enough so that, if desired, parameters
587 may be chosen such that simulated craters reproduce the mean observations (Bray et al., 2008)
588 (regardless of the thermal gradient). However, this approach would obscure the physics behind what is
589 controlling the observed crater morphologies. Instead, we chose to fix the parameters that control the
590 cratering mechanics (equation of state and strength models) and to vary other parameters: the impact
591 conditions and target properties. In Figure 6, because the cratering mechanics model for the two sets of
592 simulations is identical, we attribute the observed variation (the transition from increasing depth with
593 diameter to decreasing depth with diameter at 30 km) to be the result of the different initial thermal

594 profiles. The implicit assumption behind this approach is that the same cratering mechanics model
595 applies over the entire size range of craters studied here.

596 We also considered the sensitivity of the geometry of the hot plug to the acoustic fluidization
597 parameters (primarily the effective viscosity and decay time scale). While the mass of the hot plug is
598 independent of the acoustic fluidization parameters, the final configuration of the plug is not. For
599 example, if the acoustic fluidization viscosity is raised (less collapse), then the plug will undergo less
600 squeezing during collapse, and the final crater diameter will be smaller. Thus, the ratio of liquid plug
601 diameter to crater diameter will increase. If the acoustic fluidization viscosity is lowered (more
602 collapse), then the plug will undergo more squeezing during collapse (becoming thinner), and the final
603 crater diameter will be larger. Thus, the ratio of liquid plug diameter to crater diameter will decrease.
604 For the 2-km diameter projectile simulation (Figure 2), the ratio of hot plug diameter to crater diameter
605 (using measurement method A) was 0.18 (Figure 10). Adjusting the acoustic fluidization viscosity by one
606 order of magnitude above and below the nominal value changes the plug to crater diameter ratio to
607 0.24 and 0.10, respectively. These values are still consistent with the range of values (0.11 to 0.3)
608 measured by Alzate and Barlow (2011) and Schenk (1993). While this is compelling support for a
609 relationship between plugs and central pits, we have not modeled the evolution of the plug into a
610 central pit or dome. The shock code cannot model the necessary processes, and this important step is
611 left for future work. Variations of the decay time scale (from one half to double the nominal value) also
612 did not induce significant morphological changes in the hot plug. Over the range of acoustic fluidization
613 parameters that produce final crater depth to diameters in the observed range, the hot plug
614 morphologies are similar and the results presented in Figure 10 are robust.

615 *Composition*

616 In this work, the composition of the projectile and target was pure H₂O ice. The addition of
617 significant amounts of other materials (both other volatiles and refractory phases) will affect both the

618 equation of state and the strength model. If the target is predominantly H₂O ice, then we expect the
619 rheology to be dominated by ice. Similarly, discontinuous excavation should be present in a surface
620 primarily composed of H₂O ice. Hence, the results presented here should be widely applicable to icy
621 satellites.

622 *2D versus 3D*

623 The calculations in this work were all conducted using two-dimensional cylindrical geometries
624 and thus suffered from artifacts along the x=0 symmetry boundary condition. A few low resolution 3D
625 calculations were conducted to explore the effect of the calculation geometry and impact angle (see
626 online supplemental information). The mass and spatial distribution of the hot plug (>270 K) was
627 quantitatively similar in the 2D and 3D cases (Table S1). However, the amount of completely melted
628 material (>273.5 K) decreased in 3D. In the 2D calculations, much of the completely melted material
629 (the very high red and yellow colored temperatures along the center line of Figure 2E) is an artifact of
630 the centerline boundary. Additionally, two dimensional calculations may only consider vertical impacts.
631 Discontinuous excavation is also observed in our 3D oblique impact calculations (animations available in
632 the online supplemental information). Although the spatial distribution of shock pressures close to the
633 impact site is strongly affected by the impact angle, the shock pressure field at distances 2-3 times
634 greater than the projectile radius is nearly hemispherical (Kraus and Stewart, 2011; Pierazzo and
635 Melosh, 2000). The low shock pressures (>0.6 GPa) that are required to form the ice polymorphs
636 involved in discontinuous excavation are within the hemispherical zone for the impact velocities
637 discussed here. Hence, the formation of high-pressure polymorphs of ice will produce circular hot plugs
638 for any circular crater formed at the appropriate impact velocity (Figure 11).

639 **5. Conclusions**

640 In this work, we simulated crater formation on the icy satellite Ganymede using recent
641 improvements in the models for the equation of state and strength of H₂O ice. In particular, the model

642 equation of state includes the dense high-pressure ice polymorphs ices VI and VII. We find that the
643 shock-induced formation of these polymorphs leads to a phenomenon we call discontinuous excavation,
644 whereby a gap is created in the excavation flow. Over a certain range of impact energy and impact
645 velocity, the highly-shocked material that is interior to the discontinuity is concentrated in a hot,
646 partially liquid plug in the crater floor during crater collapse.

647 We examined the possibility that the hot plug may be genetically related to observed central
648 pits. Several observations support this proposed origin for central pits. First, the calculated geometries
649 of hot plugs are similar to observed ratios of pit width to crater diameter. Second, the range of crater
650 sizes that are dominated by central pit morphologies overlaps with calculations of when a substantial
651 hot plug of material will form in a crater floor. Third, variations in the morphology of craters of similar
652 size (with and without central pits) can be explained by differences in impact velocity. Fourth,
653 decreased amounts of rim collapse may be explained by the central plug impeding collapse. Finally, the
654 occurrence of central pits on only the largest icy satellites (without active resurfacing) is related to the
655 impact energy and velocities required to create a sufficient mass of hot material.

656 Our simulations explored the effect of varying the impact conditions and target thermal gradient
657 on impact crater formation on icy satellites. By using independently derived model parameters (quasi-
658 static strength parameters determined by laboratory experiments, acoustic fluidization parameters
659 fitted to lunar data, and an equation of state based on laboratory data), we can illustrate a diversity of
660 cratering phenomena, including the discovery of discontinuous excavation and hot plug formation. In a
661 demonstration of the reliability of the independent model input parameters, the geometry (depth and
662 diameter) of simulated craters are in good agreement with observations.

663 The simulated craters also provide some insight into the observed transition in crater depths
664 with increasing diameters on the icy Galilean satellites. The calculated crater depths begin to decrease
665 with increasing crater diameter above about 30 km when the target has a warm thermal gradient,

666 whereas crater depths continue to increase in a cold isothermal crust. The warm thermal gradient
667 calculations are in good agreement with observations on Ganymede and Callisto and support the
668 suggestion by Schenk (2002) that the transition in crater geometries is related to a rheological transition
669 within the icy satellites. Our simulations also qualitatively support the interpretation that the dramatic
670 decrease in depth for the largest craters on the icy Galilean satellites is related to the presence of a
671 subsurface ocean (Schenk, 2002; Schenk and Turtle, 2009).

ACCEPTED MANUSCRIPT

672

673 **Appendix**674 **The 5-Phase Model Equation of State for H₂O**

675 The tabular 5-phase model equation of state was developed to capture the phase changes observed on
676 the experimental ice Hugoniot (Stewart and Ahrens, 2005). The methodology used to construct the EOS
677 table is described in the appendix in Senft and Stewart (2008). The model is compared to experimental
678 boundaries for the known stable phases in Figure A1. Recent measurements of the melting curve of ice
679 VII (summarized in Dunaeva et al., 2010) are scattered and generally slightly higher than the model;
680 however, the high-pressure portion of the ice VII melting curve does not impact the results presented
681 here. The tabular equation of state is available from Stewart.

682 **Discontinuous Excavation**

683 The phenomenon of discontinuous excavation arises because of the shock-induced formation of
684 ices VI and VII and the back transformation to ice Ih. We confirmed that the observed phenomenology
685 during impact cratering simulations was robust by using a simple phase transformation equation of state
686 model (ptran in CTH). The test equation of state was composed of two Mie-Grüneisen segments that
687 represented ice Ih and a dense, high-pressure phase. The high-pressure phase transformed back to the
688 low-pressure phase upon unloading. As with the 5-Phase H₂O equation of state, a gap developed during
689 crater excavation at the location of the onset of the high-pressure phase.

690 Five segments are observed on the H₂O ice Hugoniot: ice Ih (elastic), ice Ih (shock), ice VI, ice VII,
691 and supercritical fluid (Stewart and Ahrens, 2005). The loading and release paths are dramatically
692 different between the (1) ice Ih, (2) ices VI and VII, and (3) supercritical fluid regions. These paths are
693 shown schematically in Figure A2 (for data points refer to Figure 15 in Stewart and Ahrens, 2005). Within
694 the ice Ih region, the loading and unloading paths approximately follow the Hugoniot. In the ices VI and
695 VII region, the loading path involves a significant volume compression and the release path is steep until

696 the transformation to ice Ih (dotted line). In contrast, ice shocked to supercritical fluid releases along a
 697 shallower path (dashed line).

698 In the decaying shock front during an impact event, material shocked to the supercritical fluid
 699 phase boundary at around 6 GPa is adjacent to material shocked to ice VII. Although the two parcels of
 700 material have continuous particle velocities in their peak shock states, upon release their particle
 701 velocities will diverge because of the difference in release paths. A similar process will occur at the ice
 702 Ih-ice VI transition. More generally, material is accelerated to a particle velocity, $u_{p,H}$, by the shock
 703 wave. Upon arrival of the rarefaction wave with particle velocity $u_{p,R}$, the particle velocities sum,

$$704 \quad u_p = u_{p,H} \pm u_{p,R}, \quad (1)$$

705 where the sign depends on the direction of the rarefaction wave. The values add when the rarefaction
 706 wave direction is opposite the shock wave (e.g., in a laboratory measurement of downrange free surface
 707 velocities) and subtract when the wave directions are the same, as during impact cratering. The particle
 708 velocity contribution from the isentropic rarefaction wave is given by the Riemann integral (e.g., Rice et
 709 al., 1958),

$$710 \quad u_{p,R} = \int_{P_R}^{P_H} \left(-\frac{dV}{dP} \right)^{1/2} dP = \int_{P_R}^{P_H} \frac{V dP}{c_R}, \quad (2)$$

711 where c_R is the bulk sound speed (the rarefaction wave velocity), P is pressure, V is specific volume, and
 712 S denotes isentropic release. The subscripts H and R refer to the Hugoniot and release states,
 713 respectively. Note that the slope of the release path is related to the sound speed in the shocked state;
 714 hence the steeper release from ices VI and VII reflects the larger sound speed of these phases.

715 From Equation (2) and the release paths in Figure A2, the release wave particle velocity of
 716 material shocked to point A and fully released will be larger than for material shocked to point B and
 717 released to point B', which in the simulations corresponds to the ice Ih-ice VI phase boundary. Recall
 718 that the back transformation to ice Ih is delayed during impact cratering until the volume increase may

719 be accommodated by the excavation flow. Depending on the geometry of the problem, a gap may form
720 initially between material released completely from the supercritical state (point A) and material
721 released to point B'. When the transformation from ice VI to ice Ih is finally achieved, the velocity of the
722 parcel of material released from point B' is significantly changed. Similarly, material shocked to points C
723 and D will have continuous particle velocities in the shock state and very different particle velocities
724 upon release. In the geometry of an impact cratering event, the annulus of material shocked to ices VI
725 and VII obtains fully released particle velocities sufficiently slower to result in separation of the annulus
726 from material shocked to ice Ih (point D). Hence, materials shocked to ice VI and VII are incorporated
727 into the central plug during discontinuous excavation.

728 The previous discussion focused on a single shock and single release wave. Note that the
729 impedance (density \times sound speed) contrast between ices VI and VII and the surrounding phases leads
730 to partial reflections of the rarefaction wave, which forms the tail of the detached (hemispherical shell)
731 shock. The reflecting waves also act to slow down the material in the central plug; however, the back
732 transformation from ice VI to ice Ih provides the greatest disruption to the excavation flow.

733 To illustrate the formation of a gap from the processes described above, we consider a simple
734 impact geometry: a thin plate impacting a half space. We simulated a one-dimensional impact by a 3-
735 mm sheet of ice onto a half space of ice at 15 km/s. An animation of this event is available in the online
736 supplemental materials.

737

738 **References**

- 739 Alvarells, J. L., Zahnle, K. J., Dobrovolskis, A. R., Hamill, P., 2002. Orbital evolution of impact ejecta from
740 Ganymede. *Icarus*. 160, 108-123.
- 741 Alzate, N., Barlow, N. G., 2011. Central pit craters on Ganymede. *Icarus*. 211, 1274-1283.
- 742 Artemieva, N., Lunine, J., 2003. Cratering on Titan: impact melt, ejecta, and the fate of surface organics.
743 *Icarus*. 164, 471-480.
- 744 Artemieva, N., Lunine, J., 2005. Impact cratering on Titan II. Global melt, escaping ejecta, and aqueous
745 alteration of surface organics. *Icarus*. 175, 522-533.
- 746 Barlow, N. G., 2006. Impact craters in the northern hemisphere of Mars: Layered ejecta and central pit
747 characteristics. *Meteoritics & Planetary Science*. 41, 1425-1436.
- 748 Barlow, N. G., 2007. Central pit craters on Mars and Ganymede. *Meteoritics and Planetary Science*
749 Supplement. 42, 5120.
- 750 Barlow, N. G., 2009. Martian central pit craters: summary of northern hemisphere results. *Lunar Planet.*
751 *Sci.* XL. Abstract 1915.
- 752 Bertie, J. E., Whalley, E., Calvert, L. D., 1964. Transformations of ice VI and ice VII at atmospheric
753 pressure. *Canadian J. Chem.* 42, 1373-1378.
- 754 Billings, S. E., Kattenhorn, S. A., 2005. The great thickness debate: Ice shell thickness models for Europa
755 and comparisons with estimates based on flexure at ridges. *Icarus*. 177, 397-412.
- 756 Bray, V. J., Collins, G. S., Morgan, J. V., Schenk, P. M., 2008. The effect of target properties on crater
757 morphology: comparison of central peak craters on the Moon and Ganymede. *Meteoritics &*
758 *Planetary Science*. 43, 1979-1992.
- 759 Bray, V. J., Schenk, P. M., Melosh, H. J., Collins, G. S., Morgan, J. V., 2009. Dimensions of central pits in
760 Ganymede craters. *Lunar Planet. Sci.* XL. Abstract 1350.
- 761 Chapman, C. R., McKinnon, W. B., Cratering of Planetary Satellites. In: J. A. Burns, M. S. Matthews, (Eds.),
762 Satellites. University of Arizona, 1986, pp. 492-580.
- 763 Chyba, C., 2000. Energy for microbial life on Europa. *Nature*. 403, 381-382.
- 764 Collins, G., Numerical Modeling of Large Impact Crater Collapse. Department of Earth Science and
765 Engineering, Vol. Ph.D. University of London, 2002, pp. 235.
- 766 Collins, G. S., Melosh, H. J., Ivanov, B. A., 2004. Modeling damage and deformation in impact
767 simulations. *Meteoritics & Planetary Science*. 39, 217-231.
- 768 Crawford, D. A., Adaptive mesh refinement in CTH. Technical Report SAND99-1118C. Sandia National
769 Laboratories, Albuquerque, NM, 1999, pp. 10.
- 770 Croft, S. K., 1981. On the origin of pit craters. *Lunar Planet. Sci.* XII. Abstract p. 196-198.
- 771 Croft, S. K., 1983. A proposed origin for palimpsests and anomalous pit craters on Ganymede and
772 Callisto. *Proc. Lunar Planet. Sci. Conf* 14th. p. 71-89.
- 773 DeVries, R. J., Barlow, N. G., 2009. Central pit craters in the southern hemisphere of Mars. *Lunar Planet.*
774 *Sci.* XL. Abstract 1929.
- 775 Dombard, A. J., McKinnon, W. B., 2000. Long-term retention of impact crater topography on Ganymede.
776 *Geophysical Research Letters*. 27, 3663-3666.
- 777 Dunaeva, A. N., Antsyshkin, D. V., Kuskov, O. L., 2010. Phase Diagram of H₂O: Thermodynamic Functions
778 of the Phase Transitions of High-Pressure Ices. *Solar System Research*. 44, 202-222.
- 779 Feistel, R., Wagner, W., 2007. Sublimation pressure and sublimation enthalpy of H₂O ice Ih between 0
780 and 273.16 K. *Geochimica et Cosmochimica Acta*. 71, 36-45.

- 781 Golombek, M. P., Banerdt, W. B., 1986. Early thermal profiles and lithospheric strength of Ganymede
782 from extensional tectonic features. *Icarus*. 68, 252-265.
- 783 Greeley, R., Find, J. H., Gault, D. E., Guest, J. E., Impact cratering on icy satellites. In: D. Morrison, (Ed.),
784 Satellites of Jupiter. University of Arizona Press, Tucson, AZ, 1982, pp. 340-378.
- 785 Kraus, R. G., Stewart, S. T., 2011. Impacts onto H₂O Ice: Scaling Laws for Melting, Vaporization,
786 Excavation, and Final Crater Size. *Icarus*. submitted.
- 787 Luttrell, K., Sandwell, D., 2006. Strength of the lithosphere of the Galilean satellites. *Icarus*. 183, 159-
788 167.
- 789 McGlaun, J. M., Thompson, S. L., Elrick, M. G., 1990. CTH: a three-dimensional shock wave physics code.
790 *International Journal of Impact Engineering*. 10, 351-360.
- 791 Melosh, H. J., 1979. Acoustic fluidization: a new geologic process? *Journal of Geophysical Research*. 84,
792 7513-7520.
- 793 Melosh, H. J., Ivanov, B. A., 1999. Impact crater collapse. *Annual Reviews of Earth and Planetary Science*.
794 27, 385-415.
- 795 Melosh, J., 1989. Impact cratering: A geologic process. Oxford University Press, New York.
- 796 Moore, J. M., Malin, M. C., 1988. Dome craters on Ganymede. *Geophysical Research Letters*. 15, 225-
797 228.
- 798 Moore, J. M., et al., 2001. Impact features on Europa: Results of the Galileo Europa Mission (GEM).
799 *Icarus*. 151, 93-111.
- 800 Moore, J. M., Schenk, P. M., Bruesch, L. S., Asphaug, E., McKinnon, W. B., 2004. Large impact features on
801 middle-sized icy satellites. *Icarus*. 171, 421-443.
- 802 Ormo, J., Shuvalov, V. V., Lindstrom, M., 2002. Numerical modeling for target water depth estimation of
803 marine-target impact craters. *Journal of Geophysical Research*. 107, doi:10.1029/2002JE001865.
- 804 Passey, Q. R., Shoemaker, E. M., Craters and basins on Ganymede and Callisto: Morphological indicators
805 of crustal evolution. In: D. Morrison, (Ed.), Satellites of Jupiter. University of Arizona Press,
806 Tucson, 1982, pp. 379-434.
- 807 Petrenko, V. F., Whitworth, R. W., 1999. Physics of ice. Oxford U., New York.
- 808 Pierazzo, E., Vickery, A. M., Melosh, H. J., 1997. A re-evaluation of impact melt production. *Icarus*. 127,
809 408-423.
- 810 Pierazzo, E., Melosh, H. J., 2000. Melt production in oblique impacts. *Icarus*. 145, 252-261.
- 811 Pike, R. A., 1976. Crater dimensions from Apollo data and supplemental sources. *Moon*. 15, 463-477.
- 812 Rice, M. H., McQueen, R. G., Walsh, J. M., Compression of solids by strong shock waves. In: F. Seitz, D.
813 Turnbull, Eds.), *Solid State Physics Vol. 6*. Academic Press, New York, 1958, pp. 1-63.
- 814 Schenk, P. M., 1991. Ganymede and Callisto: Complex crater formation and planetary crusts. *Journal of*
815 *Geophysical Research*. 96, 15635-15664.
- 816 Schenk, P. M., 1993. Central pit and dome craters: exposing the interiors of Ganymede and Callisto.
817 *Journal of Geophysical Research*. 98, 7475-7498.
- 818 Schenk, P. M., 2002. Thickness constraints on the icy shells of the Galilean satellites from a comparison
819 of crater shapes. *Nature*. 417, 419-421.
- 820 Schenk, P. M., Chapman, C. R., Zahnle, K., Moore, J. M., Ages and interiors: the cratering record of the
821 Galilean satellites. In: F. Bagenal, et al., Eds.), *Jupiter: The planet, satellites, and magnetosphere*.
822 Cambridge University Press, Cambridge, UK, 2004, pp. 427-456.
- 823 Schenk, P. M., Turtle, E. P., Europa's Impact Craters: Probes of the Icy Shell. In: R. T. Pappalardo, et al.,
824 Eds.), *Europa*. U. Arizona Press, Tucson, 2009, pp. 181-198.
- 825 Schubert, G., Anderson, J. D., Spohn, T., McKinnon, W. B., Interior composition, structure, and dynamics
826 of the Galilean satellites. In: F. Bagenal, et al., Eds.), *Jupiter: The Planet, Satellites, and*
827 *Magnetosphere*. Cambridge University Press, Cambridge, United Kingdom, 2004, pp. 281-306.

- 828 Senft, L. E., Stewart, S. T., 2007. Modeling impact cratering in layered surfaces. *Journal of Geophysical*
829 *Research*. 112, doi: 10.1029/2007JE002894.
- 830 Senft, L. E., Stewart, S. T., 2008. Impact crater formation in icy layered terrains on Mars. *Meteoritics and*
831 *Planetary Science*. 43, 1993-2013.
- 832 Senft, L. E., Stewart, S. T., 2009. Dynamic Fault Weakening and the Formation of Large Impact Craters.
833 *Earth and Planetary Science Letters*. 287, 471-482.
- 834 Showman, A. P., Malhotra, R., 1999. The Galilean satellites. *Science*. 286, 77-84.
- 835 Smith, B. A., et al., 1979. The Galilean Satellites and Jupiter: Voyager 2 Imaging Science Results. *Science*.
836 206, 927-950.
- 837 Spohn, T., Schubert, G., 2003. Oceans in the icy Galilean satellites of Jupiter? *Icarus*. 161, 456-467.
- 838 Stewart, S. T., Ahrens, T. J., 2005. Shock properties of H₂O Ice. *Journal of Geophysical Research*. 110, doi:
839 10.1029/2004JE002305.
- 840 Stewart, S. T., Seifert, A., Obst, A. W., 2008. Shocked H₂O ice: Thermal emission measurements and the
841 criteria for phase changes during impact events. *Geophysical Research Letters*. 35, doi:
842 10.1029/2008GL035947.
- 843 Thompson, S. L., Lauson, H. S., Improvements in the Chart D Radiation-Hydrodynamic CODE III: Revised
844 Analytic Equations of State, Sandia Report #SC-RR-710714. Sandia Laboratories, Albuquerque,
845 NM, 1972.
- 846 Turtle, E. P., Pierazzo, E., 2001. Thickness of a European ice shell from impact crater simulations.
847 *Science*. 294, 1326-1328.
- 848 Turtle, E. P., Ivanov, B. A., 2002. Numerical simulations of impact crater excavation and collapse on
849 Europa: implications for ice thickness. *Lunar Planet. Sci.* XXXIII. Abstract 1929.
- 850 Wagner, W., Pruss, A., 2002. The IAPWS formulation 1995 for the thermodynamic properties of ordinary
851 water substance for general and scientific use. *Journal of Physical and Chemical Reference Data*.
852 31, 387-535.
- 853 Williams, K. K., Zuber, M. T., 1998. Measurement and analysis of lunar basin depths from Clementine
854 altimetry. *Icarus*. 131, 107-122.
- 855 Wood, C. A., Head, J. W., Cintala, M. J., 1978. Interior morphology of fresh Martian craters: The effects
856 of target characteristics. *Proc. Lunar Planet. Sc. Conf.* 9th. 3691-3709.
- 857 Wood, C. A., et al., 2010. Impact craters on Titan. *Icarus*. 206, 334-344.
- 858 Wünnemann, K., Ivanov, B. A., 2003. Numerical modelling of the impact crater depth-diameter
859 dependence in an acoustically fluidized target. *Planetary and Space Science*. 51, 831-845.
- 860 Zahnle, K., Dones, L., Levison, H., 1998. Cratering rates on the Galilean satellites. *Icarus*. 136, 202-222.
- 861 Zahnle, K., Schenk, P., Levison, H., Dones, L., 2003. Cratering rates in the outer solar system. *Icarus*. 163,
862 263-289.
- 863

864

865 **Figure Captions**

866 *Figure 1:* Depth versus diameter measurements for fresh craters on the icy Galilean satellites: Callisto
867 (A), Ganymede (B), and Europa (C). Thick black lines are fits to lunar data, symbols are data points for
868 the icy satellites, and thin lines are fits through the data. The dashed line in C is the Ganymede fit.
869 Simple craters are plotted as solid dots, central peak craters as open circles, central pit and dome craters
870 as crosses, and anomalous forms and multiring basins as error bars. Note that error bar for the one
871 anomalous crater plotted for Callisto is representative of the size of the error bars for the data points
872 where no error bar is plotted. Figure is taken from Schenk (2002). In A, Transitions I and II and III
873 (Schenk's terminology for the observed "kinks" in the depth to diameter data) are identified.

874 *Figure 2:* Impact of a 2-km diameter projectile onto a 120-K isothermal Ganymede at 15 km/s using the
875 5-Phase EOS (A-E) and the Mie-Grüneisen EOS (no phase changes) for ice Ih (F-J). A-D and F-I show
876 density at different times during crater formation, and the black dots are initially horizontal rows of
877 Lagrangian tracer particles. Gray material is partially/fully vapor with densities between 0.0001 and 0.9
878 g/cm^3 . In A-D, ice Ih is indicated by dark blue, ices VI and VII as red, and liquid water as light blue and
879 green. Triangle and square points correspond to data in Figure 4A and B, respectively. E and J show
880 temperature at 400 s; temperatures in J are unreliable. Also, the high temperatures (colored red and
881 yellow) along the centerline of E are an artifact due to the symmetry boundary condition. The black line
882 in E is the 270 K contour (hot plug), and the dashed line shows the central plug boundary (on one side).
883 Spatial, density, and temperature scales are the same both columns. Final craters are about 40 km in
884 diameter. See supplemental material for animations.

885 *Figure 3:* Schematic of an impact cratering event on an icy satellite analogous to the simulation shown in
886 Figure 2A. Panels do not have the same scale. (A) Initial locations of material undergoing shock-induced

887 phase changes (sf is supercritical fluid; high pressure phases are ices VI and VII). (B) The impedance
 888 mismatch between the high-pressure phases and lower density phases (liquid above and ice Ih below)
 889 leads to a discontinuity in the crater excavation flow. The rarefaction wave only partially decompresses
 890 the high-pressure phases (to the phase boundary); complete decompression is achieved when the
 891 excavation flow allows for the volume expansion into ice Ih. The material at the discontinuity releases
 892 to the ice Ih-vapor boundary. (C) During crater collapse, the most highly shocked material is
 893 concentrated and compressed in a central plug defined by a stratigraphic discontinuity (colored in gray)
 894 in the crater floor. A hot plug of material (>270 K) is concentrated within the central plug.

895 *Figure 4:* Example Lagrangian tracer paths (colored points) from simulation shown in Figure 2A plotted
 896 on the simplified H₂O phase diagram of the 5-Phase EOS. Symbol colors indicate time from 0 s (purple)
 897 to 180 s (red). A. The material is shocked first to the elastic precursor state (ep) and then to 0.74 GPa,
 898 releases to the ice VI/liquid boundary and down to the Ice VI/liquid/ice Ih triple point, where it remains
 899 at the triple point until expansion into ice Ih can be accommodated by the excavation flow, after which
 900 it continues decompressing to the ice Ih/vapor boundary. The material is slightly pressurized during
 901 crater collapse. Initial location was $x = 2.38$ km, $y = -7.5$ km, and location at 400 s was $x=1.9$ km, $y=-6.95$
 902 km (triangle point in Fig. 2A-D). B. The material was shocked to 11.15 GPa, released to the saturation
 903 vapor curve and down to the triple point. The material was pressurized along the melting curve during
 904 crater collapse. Initial location was $x = 1.38$ km, $y = -3.75$ km, and location at 400 s was $x=6.48$ km, $y=-$
 905 1.89 km (square point in Fig. 2A-D).

906 *Figure 5:* Mass of hot plug versus crater diameter for a cold and a warm thermal profile. The volume of
 907 the hot plug is defined by the 270 K temperature contour (thin lines) and represents partial melt.
 908 Power law fits for the 270 K contour masses are as follows: $m = 10^{7.75} D^{4.03}$ for the cold case, and
 909 $m = 10^{8.20} D^{3.83}$ for the warm case (m is the mass of the hot plug in kg and D is the diameter in km).

910 *Figure 6:* Depth versus diameter data for Ganymede compared with simulation results for warm and
911 cold thermal gradients. The depth versus diameter curve for the Earth's moon is also shown for
912 comparison (dashed line with no points). Diameters are rim-to-rim diameters and depths are rim-to-
913 floor depths. The shaded area shows the range of measurements from Schenk (2002). Connected
914 points are simulations that used acoustic fluidization to aid crater collapse; unconnected points utilized
915 only the quasi-static strength model.

916 *Figure 7:* Time series of impacts of a 5-km diameter projectile onto Ganymede at 15 km/s with a cold
917 (120 K isothermal) (left column) and a warm (convective) thermal gradient (right column). Stratigraphic
918 deformation is illustrated by initially horizontal rows of Lagrangian tracer particles (black points). Colors
919 correspond to density. The scale is the same in all panels. The final crater diameters are about 105 km
920 (cold geotherm) and about 145 km (warm geotherm). See supplemental material for animations.

921 *Figure 8:* Time series of impacts of a 10-km diameter projectile onto Ganymede at 15 km/s with a warm
922 thermal gradient and an ocean at 25 km (A-E) and 50 km (F-J) depth. Stratigraphic deformation is
923 illustrated by initially horizontal rows of Lagrangian tracer particles (black points). Colors correspond to
924 density. The scale is the same in all panels. See supplemental material for animations.

925 *Figure 9:* Examples of central pit craters on Ganymede: Isis crater, 73 km in diameter (A); Sebek crater,
926 64 km in diameter (B); and Bes crater, 62 km in diameter (C). (Voyager images FDS 20640.33, 16405.48,
927 and 20637.41.)

928 *Figure 10:* Ratio of hot plug width to crater diameter versus crater diameter for a cold and warm thermal
929 gradient. In A, plug width is defined as the width of the part of the plug that extends to depth, labeled
930 B in Figure 3C. In B, plug width is defined as the width of the plug at the surface, labeled A in Figure 3C.
931 Arrows on the right show the range of central pit diameter to crater diameter ratios found on

932 Ganymede (0.11-0.38), and the dot shows the mean (0.19). Ganymede data is from Alzate and Barlow
933 (2011).

934 *Figure 11:* Mass of hot plug versus impact velocity for impacts onto a target with a warm and a cold
935 thermal gradient. The impactor size was varied such that the amount of kinetic energy was the same.
936 For the 15 km/s impacts, the impactor was 2 km in diameter.

937 *Figure A1.* Comparison of 5-phase equation of state model with experimental phase boundaries of H₂O.
938 A. Model phase boundaries with model ice Hugoniot starting at 120 K (thick black line) and 263 K (grey
939 dashed line). B. Experimental phase boundaries as summarized in Dunaeva et al. (2010), Feistel and
940 Wagner (2007), and Wagner and Pruss (2002). Model boundaries that deviate from experiments are
941 shown as grey dashed lines.

942 *Figure A2.* Schematic of the H₂O ice Hugoniot (thick line segments). Example loading and release paths
943 are illustrated for ice shocked to the supercritical fluid (SF) phase boundary (point A, dashed lines) and
944 ice VII (point B, dotted lines).

945 **Table**

Variable	Description	Ice Parameters
Y_0	shear strength of intact rock at zero pressure and low temperatures	10 MPa
Y_m	limiting shear strength as pressure increases at low temperatures	115 MPa
Y_c	cohesion at zero pressure and low temperature	0 MPa
μ_i	coefficient of internal friction of intact rock	2.0
$\mu_{d,l}$	coefficient of friction of fragmented rock (low pressure)	0.55
$\mu_{d,h}$	coefficient of friction of fragmented rock (high pressure)	0.2
$P_{tr,d}$	transition pressure between $\mu_{d,l}$ and $\mu_{d,h}$	10 MPa
T_m	melting temperature	273.15 K until 623 MPa, then increases at a rate of 27.19 K/GPa
ξ	thermal softening parameter	1.84
Y_{t0}	maximum tensile strength	-0.17 MPa
P_{bd}	brittle to ductile transition pressure	498 MPa
P_{bp}	brittle to plastic transition pressure	508 MPa
K_0	bulk modulus at ambient pressure and temperature	8.9 GPa
G	shear modulus at ambient pressure and temperature	3.52 GPa
D_{s0}	initial shear damage	0.0
D_{t0}	initial tensile damage	0.0
η	acoustic fluidization viscosity	$0.1 * C_s * r_p * \rho$
τ	acoustic fluidization decay constant	$150 * \left(\frac{r_p}{C_s}\right)$
C_{vib}	maximum vibration particle velocity (fraction of the maximum velocity)	0.25

946

947 **Table 1:** Quasi-static strength and acoustic fluidization parameters used to model H₂O ice. r_p is the radius of the projectile, C_s is
948 the sound speed in ice (2.3 km/s), and ρ is the density of ice (0.932 g/cm³). For a complete description of the strength model,
949 refer to Senft and Stewart [2007].

950

951 **Highlights**

952 **Modeling the morphological diversity of impact craters on icy satellites**

953 Laurel E. Senft and Sarah T. Stewart

954

- 955 • We model impact crater formation in ice using a new equation of state and rheology.
- 956 • Dynamic phase changes lead to a new phenomenon called discontinuous excavation.
- 957 • Partial melts are concentrated in a central plug, a possible precursor to pits.
- 958 • Diverse crater morphologies reflect subsurface temperature profiles.

959

ACCEPTED MANUSCRIPT

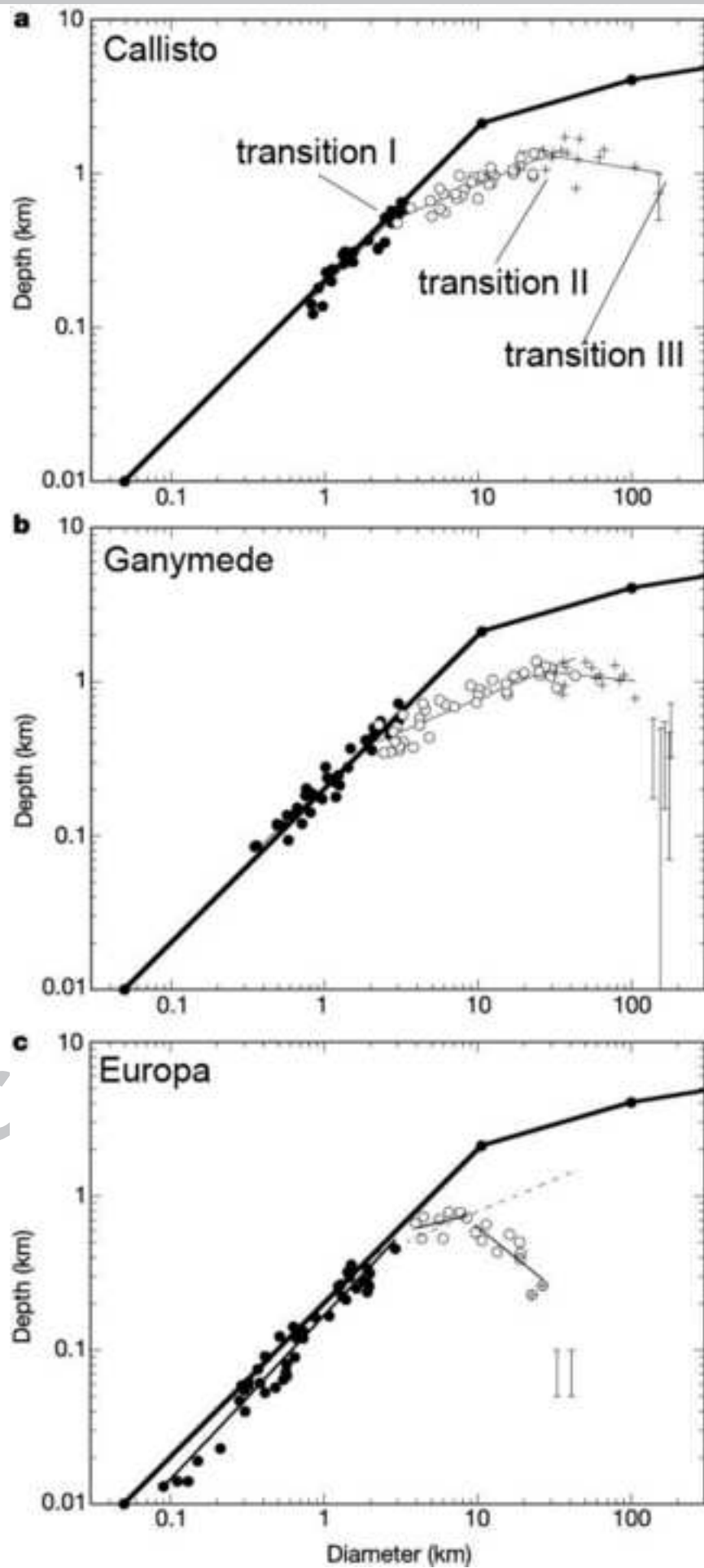
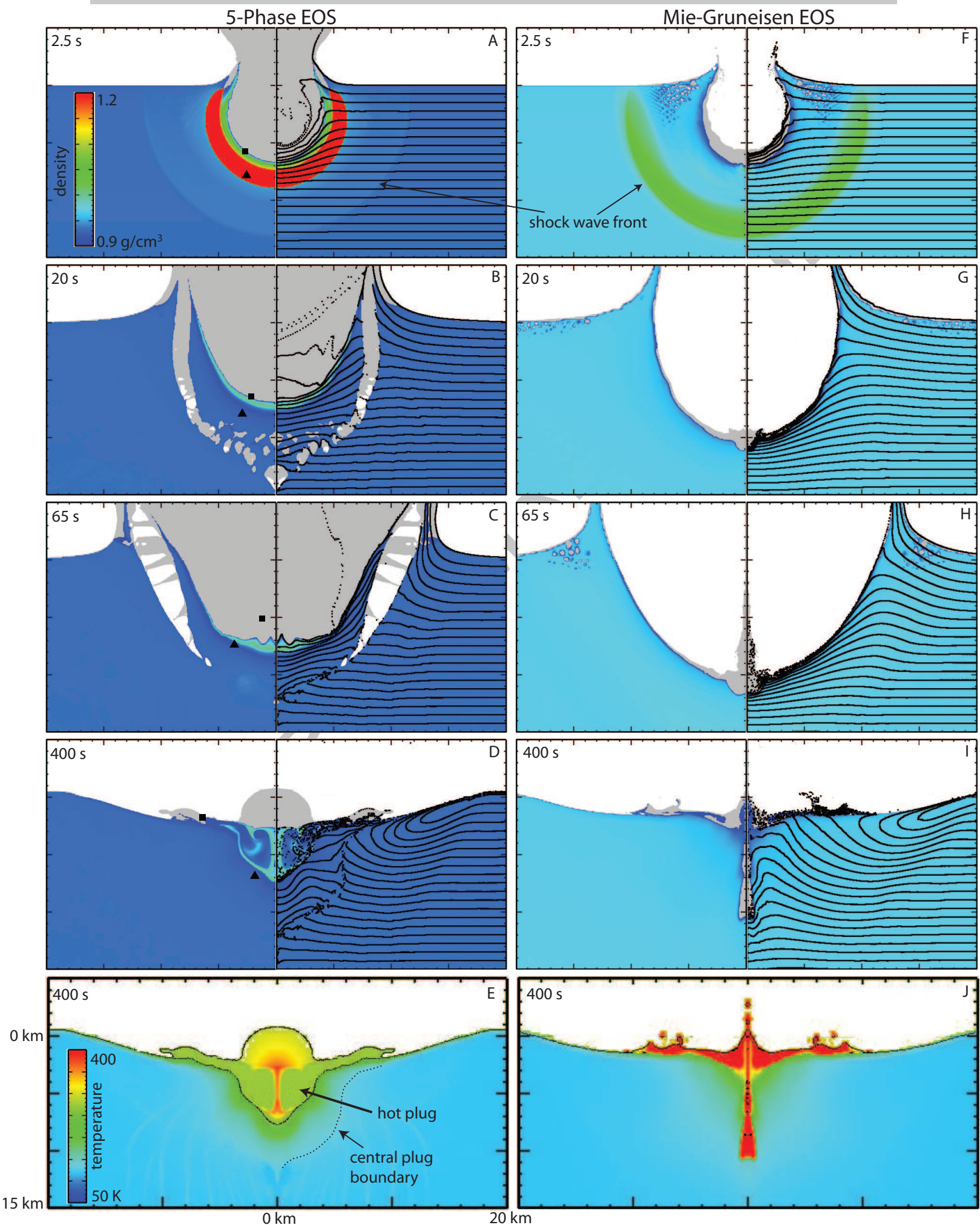


Figure 2

ACCEPTED MANUSCRIPT



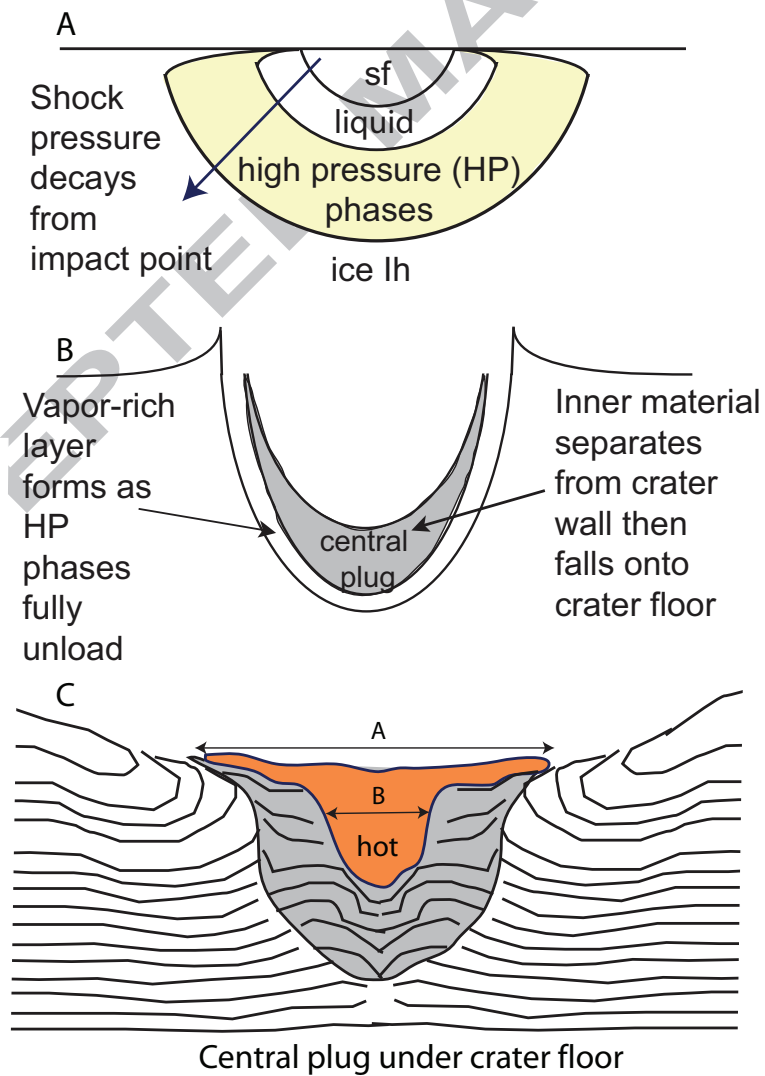
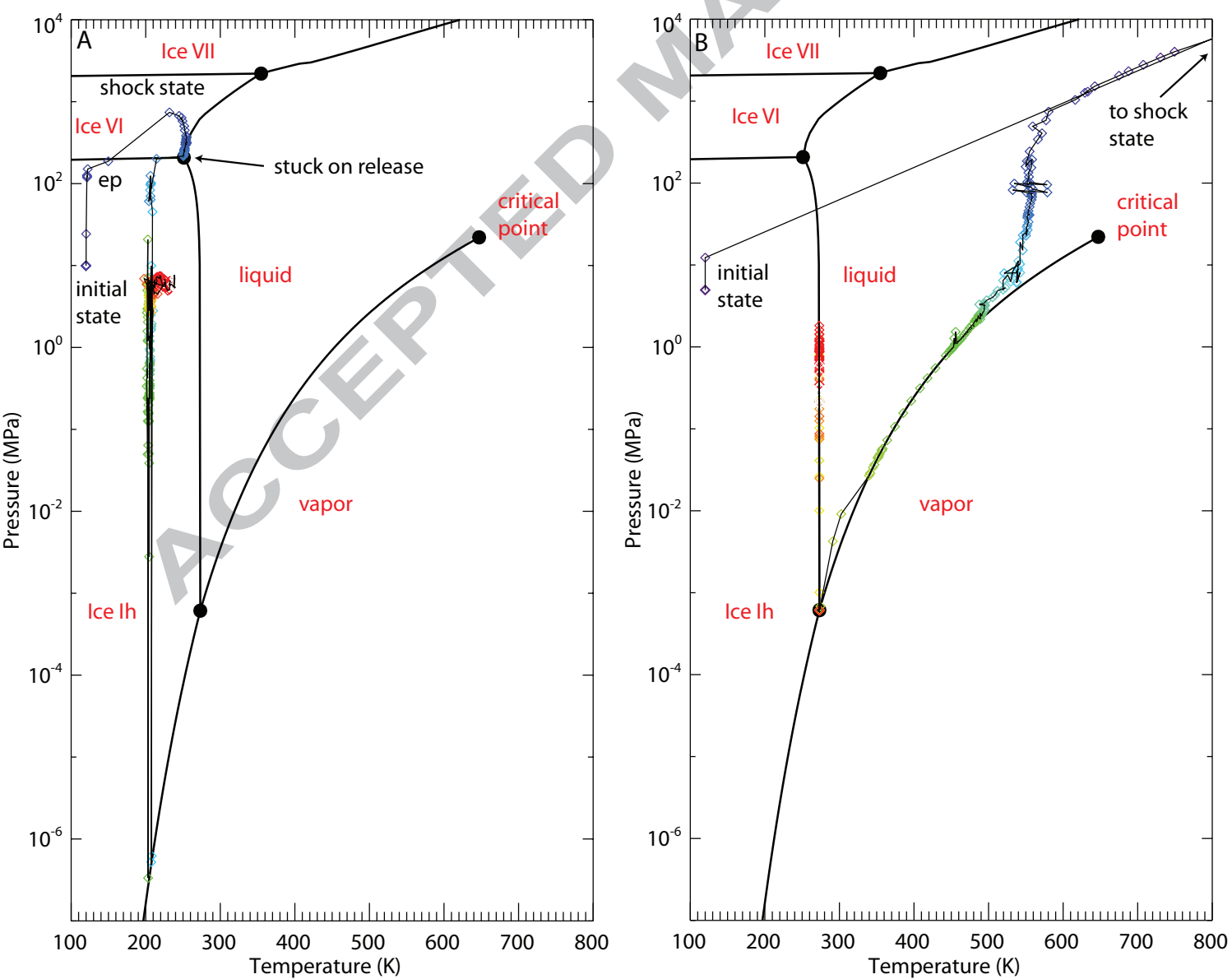
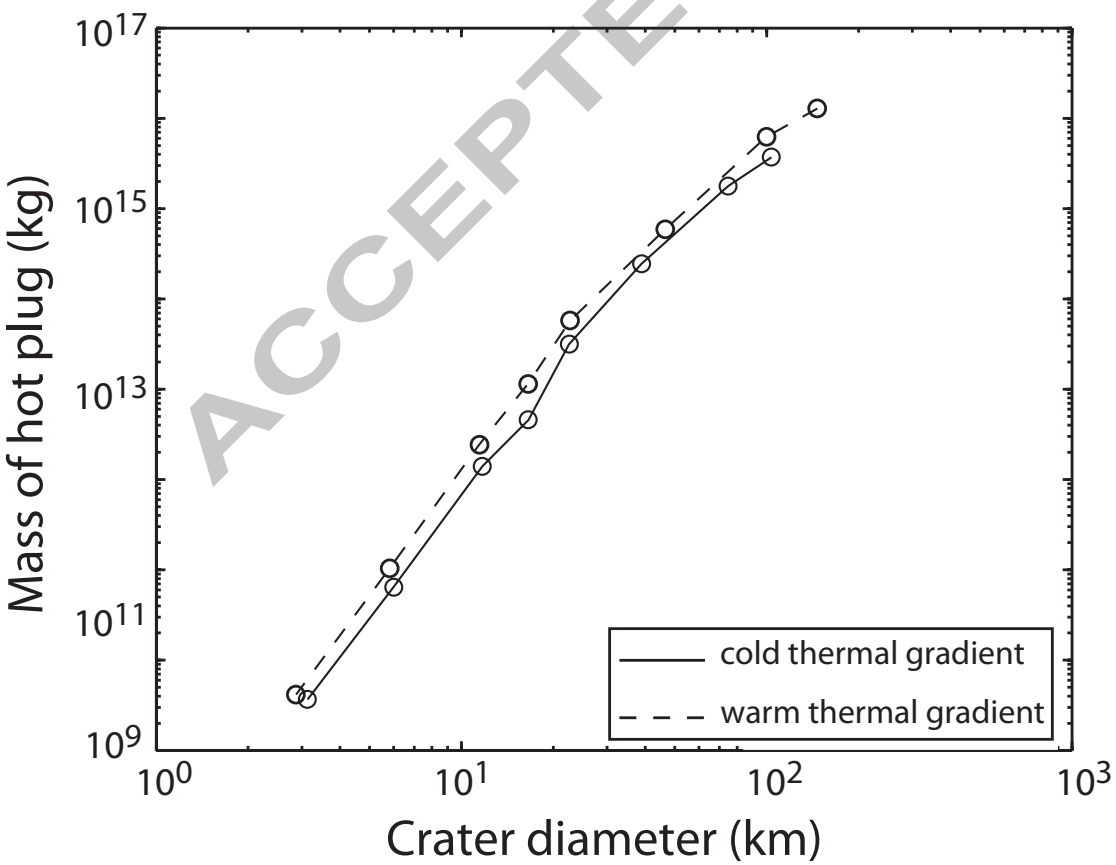


Figure 4





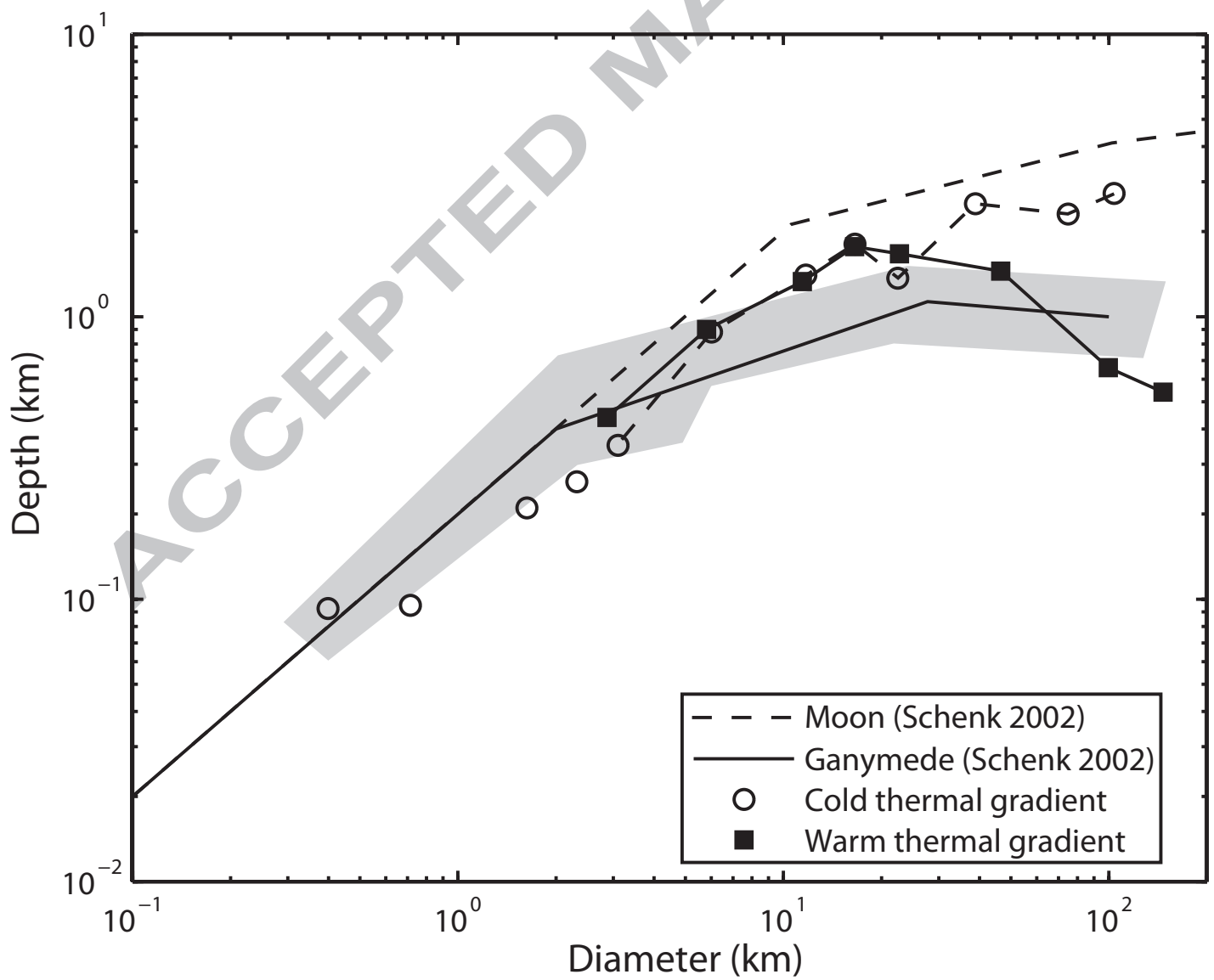
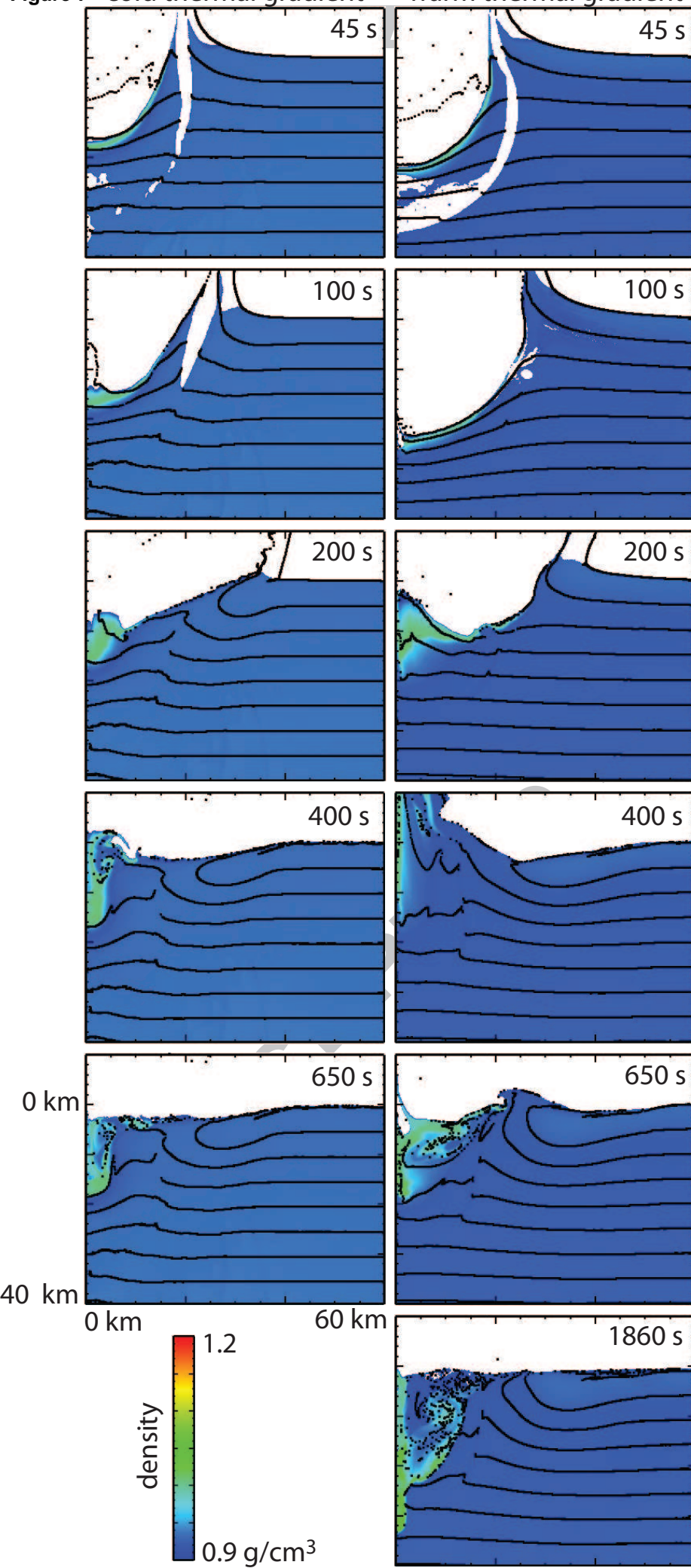


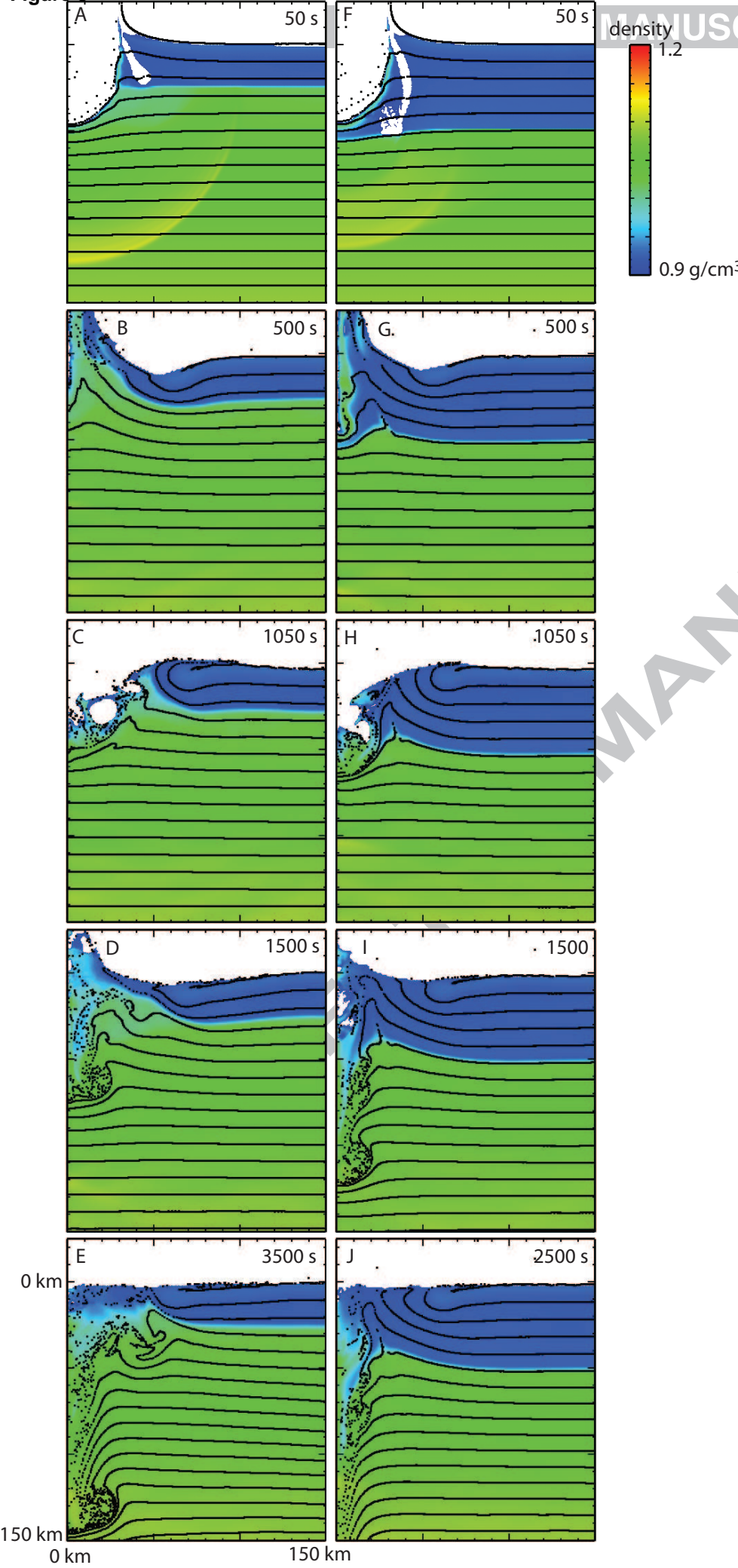
Figure 7 cold thermal gradient warm thermal gradient



MANUSCRIPT

MANUSCRIPT

Figure 8 ocean at 25 km depth ocean at 50 km depth



MANUSCRIPT

